# Magnetic Pulse Welding of Mg Sheet

by

Alexander Berlin

A thesis
presented to the University of Waterloo
in fulfillment of the
thesis requirement for the degree of
Master of Applied Science
in
Mechanical Engineering

Waterloo, Ontario, Canada, 2011

# Author’s Declaration

I hereby declare that I am the sole author of this thesis. This is a true copy of the thesis, including any required final revisions, as accepted by my examiners.

I understand that my thesis may be made electronically available to the public.

Alexander Berlin

# Abstract

Because of its low density and high strength, magnesium (Mg) and its alloys are being sought after in the automotive industry for structural applications. Although many road-going cars today contain cast Mg parts, in the fabrication of chassis structural members the wrought alloys are required. One of the challenges of fabrication with wrought Mg is welding and joining the formed sheets. Because of the commonly observed difficulties in fusion welding of Mg such as hot cracking and severe Heat Affected Zone (HAZ), this work aimed to establish the feasibility of the solid-state process Magnetic Pulse Welding in producing lap welds of Mg sheet.

Mg AZ31 alloy sheets have been lap-welded with Magnetic Pulse Welding (MPW), an Impact Welding technique, using H-shaped symmetric coils connected to a Pulsar MPW-25 capacitor bank. MPW uses the interaction between two opposing magnetic fields to create a high speed oblique collision between the metal surfaces. The oblique impact sweeps away the contaminated surface layers and forces intimate contact between clean materials to produce a solid-state weld. Various combinations of similar and dissimilar metals can be welded using MPW. Other advantages of MPW are high speed, high strength, and the possibility of being mounted on a robotic arm. The present research focuses on the feasibility and mechanical performance of an MPW weld of 0.6 mm AZ31 Mg alloy sheets made in a lap joint configuration.

Tensile shear tests were carried out on the joints produced. Load bearing capacity showed linear increase with capacitor bank discharge energy up to a certain value above which a parabolic increase was seen. Strength was estimated to be at least as high as base metal strength by measuring the fracture surface area of selected samples. The fracture surface of samples welded at higher discharge energy showed two regions. In the beginning of the bond a platelet-featured fracture brittle in appearance and a ductile, micro-voiding fracture in the latter part.

The joint cross section morphology consisted of a flattened area that had two symmetric bond zones 1 mm wide each separated by an unbonded centre zone ~3mm wide. Reasons for the

morphology were presented as a sequence of events based on the transient nature of the oblique collision angle.

The interface microstructure was studied by optical and electron microscopy. Examination of the bonds has revealed sound and defect free interfaces. No microcracking, porosity, resolidification, or secondary phase formation was observed. Metallographic examination of the unbonded centre zone revealed anisotropic deformation and a lack of cleaning from the interface. This zone is formed as a result of normal impact in the initial stage of collision. The bond zone interface of the joint was characterized by a smooth interface consisting of refined grains. In samples welded at higher energy interfacial waves developed in the latter half of the bond zone. Transmission electron microscopy (TEM) of the bond zone revealed a continuous interface having an 8-25 μm thick interlayer that coincided with the waves and had a dislocation cell structure and distinct boundaries with adjacent material. Equiaxed 300 nm dynamic recrystallized (DRX) grains were found adjacent to the interlayer as well as other slightly larger elongated grains. The interlayer is thought to be formed in plasticized state at elevated temperature through severe shear strain heating. The interlayer corresponds to a ductile fracture surface and, along with the interfacial waves, is responsible for the joint's high strength.

*Keywords:* Magnesium alloy; Ultra fine grain; Microstructure; Magnetic pulse welding

# Acknowledgments

All praise and thanks are due to God. Moreover, I wish to thank my supervisor, Dr. Y. Norman Zhou, whose vast welding experience imparted wisdom in advising. Gratitude is also owing to my other supervisors: Prof. Tam Nguyen and Prof. Michael Worswick for their support in every aspect of this work which was tremendously helpful.

Additionally I express my sincere thanks to J. Imbert, Dr. Xiao, L. Liu, A. Nasiri, Dr. Nayak, and the rest of the Centre for Advanced Materials Joining members for experimental and theoretical assistance in many aspects of the work.

I would like to thank P. Charest and J. Brent at Promatek Research Centre of Cosma for their permitting our use of their MPW machine and providing assistance with welding there.

This research is financially supported by the Natural Sciences and Engineering Research Council (NSERC) of Canada in the framework of the MagNET (Magnesium Network) Strategic Network program. Material donations from South Korea's Posco Company are greatly appreciated.

*In the name of Allah, the Most Gracious, the Most Merciful*

# Table of Contents

# List of Figures

# Chapter 1: Introduction and Background

## 1.1. Background

MPW can be classified as an Impact Welding technique which in general is a set of processes that utilize a rapid energy source to accelerate and cause collision between two metal surfaces. The collision must take place at a high enough velocity to achieve bonding through contaminant and oxide removal. Cleaning takes place via a phenomenon known as jetting which occurs as a result of shear strain localization at the interface [1]. For jetting to take place the impact must occur at an oblique angle. The sheet surfaces must make contact at a small angle, typically at least 4°, up to ~30°. This creates a single dynamic collision point that travels along the surfaces as they collide and bend flat against one another. A high pressure surrounds the collision point ejects surface material forwards, in a high velocity jet. Different sources of driving pressure are used in impact welding such as chemical explosives in Explosion Welding (EXW) or the repulsive interaction between strong pulsed magnetic fields, as in the case of Magnetic Pulse Welding (MPW). When a high current is passed through a coil adjacent to the sheet, but electrically isolated from it, its magnetic field repels the field of the generated eddy currents in the sheet. With the coil rigidly supported, the sheet can be propelled at another.

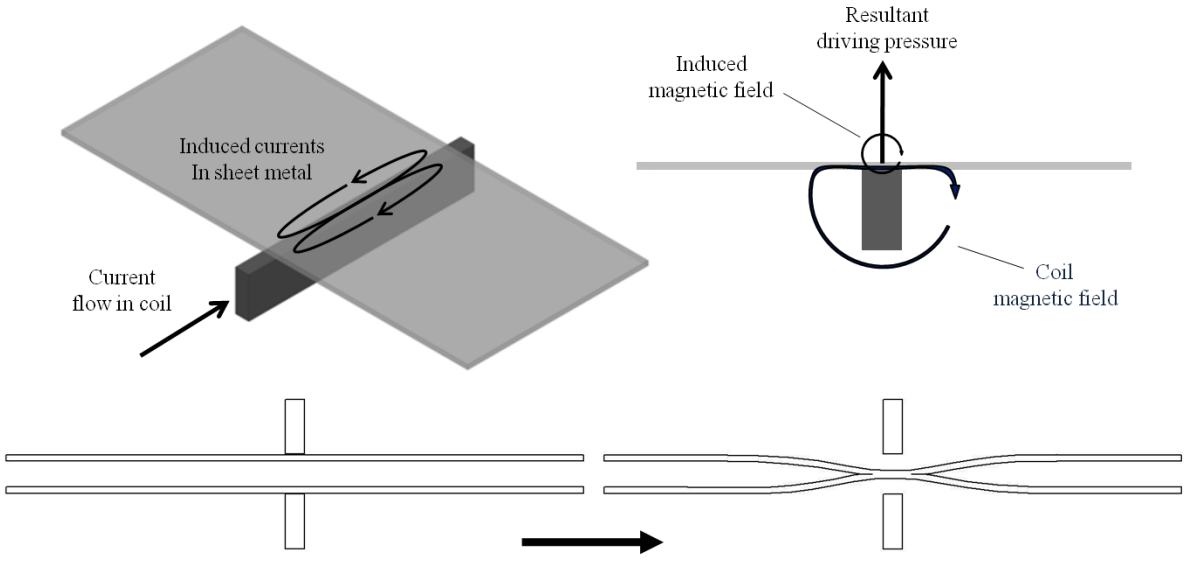


Figure 1.1: Schematic of the Magnetic Pulse Welding process

## 1.2. Magnetic Pulse Welding of Wrought Mg Alloy

Cast Magnesium (Mg) parts are already on the road in production vehicles, in the form of under hood parts and non-structural body components such as boot-lids. However, there is an increasing interest in the automotive industry to use wrought Magnesium alloys in the front end and chassis members. That is because the density of Mg is ⅔ the density of Aluminum (Al) (Al density is ⅓ that of steel) [2]. The most common wrought alloy in sheet form is AZ31B which was used in this work and which can have tensile strength as high as 287 MPa [3], making it the lightest structural metal. However, in order to switch any application to Mg alloy, several material specific manufacturing problems must first be overcome. Especially in chassis construction, along with formability, one of the major obstacles is the welding and joining these alloys. As is widely documented, fusion welding of Mg alloys is exceptionally difficult due to the formation of defects such as porosity, hot cracking, alloying element segregation, oxide inclusions, and severe softening of the Heat Affected Zone (HAZ). These fusion-related welding problems can be overcome by utilizing solid state joining processes such as Magnetic Pulse Welding. Along with the fact that MPW is the only type of Impact Welding equipment that could be mounted on a robot, other potential advantages may be [4]: base-metal like bond strength, extremely high speed, dissimilar metal combination, no filler or shielding gas, and no HAZ.

Although Impact Welding is a mature and well documented process, particularly in the case of EXW, at present there is no report on the joining of Mg to Mg, as well as little on joining Mg to other metals. This is most likely due to magnesium's complicated and often reluctant plastic deformation behaviour which does not lend itself well to the heavy strain of solid state welding processes. Moreover, due to the current early developmental state of MPW there is a lack of knowledge in the areas of weldability, joint formation, and microstructure-mechanical property correlation. In improving the understanding of the effect of microstructure on strength an approach can be made to improve the practicality of the joint and process.

## 1.3. Objectives

The objective of this thesis is to study the similar-material impact welds formed by the MPW process of AZ31B Mg alloy sheet through examining the process, weld microstructure,

and mechanical properties of the joint. Specifically, MPW was utilized to establish the feasibility of joining the Mg alloy sheet to itself. Metallurgical analysis was conducted to characterize the microstructures at various locations within the bonded joint. And the observed interface microstructure was then linked to the mechanical properties. Additionally, the joint morphology and formation was confirmed through microstructure observation.

## 1.4. Thesis Outline

This thesis is organized in six chapters. Chapter 2 presents a literature review of the fundamentals of Impact welding, the MPW process, and Mg. Chapter 3 provides a detailed experimental procedure, and explanation and operation of the technical equipment used. Chapter 4 shows the results produced. Chapter 5 is a discussion of the key results, their connection to the objectives, and their implications in light of prior research and practical application. Finally chapter 6 summarises the prominent conclusions and presents recommendations for future research in Mg MPW.

# Chapter 2: Literature Review

## 2.1. Impact Welding

### 2.1.1. Jetting and Oblique Collision

The phenomenon of impact welding was first discovered shortly after WWI when bomb shrapnel was found to have been cold-welded to metal surfaces of tanks and artillery [1]. The first application evolved into a cladding operation, known as Explosion Welding which is shown in Figure 2.1. In EXW, by 1953 the time-displacement curves of the propelled flyer plate have been characterized [5] and by 1963 the phenomenon of jetting was thoroughly modelled analytically based on geometric setup and cladding plate materials, as is summed up in the work of Cowan *et al.* [6].

EXW quickly became the most common application of Impact welding and was best known for its capability to directly join a wide variety of both similar and dissimilar combinations of metals; materials that were otherwise difficult to join because of dramatically different melting points or other complications such as reactivity with atmosphere or gross fusion defects.

Typically for Impact welding, materials are set up separated by a gap in either sheet or concentric tube configurations. An energy source (explosives, magnetic repulsion, air-gun, projectile, etc) is then used to accelerate either one or both components towards each other. Velocities at impact ($V_P$) are on order of hundreds of metres per second. The impact angle, β, has the range of ~4°-30°.

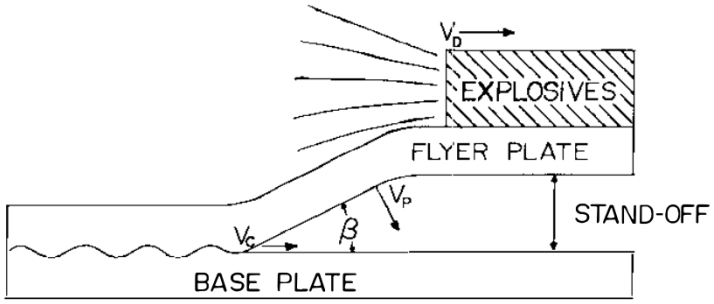


Figure 2.1: Typical, asymmetric explosion welding configuration [7].

It is generally accepted that for bonding to occur under the impact, the collision must be of a very high velocity and oblique in geometry. Whereas a normal impact of the surfaces would only result in rebound, in an oblique collision the material flows together and a very high velocity jet is emitted from the high pressure collision region cumulative of both faying surface materials (given material subsonic collision point speed). This is best shown in a reference frame that is stationary with the collision point, which is the point 'S' in Figure 2.2. The two metal plates, twice bent, that are advancing into the region are called the salient jets; the material flow that is separated, rotated, and ejected by the high pressure is called the re-entrant jet, or simply, the jet. In most seam and spot impact welding applications, as opposed to explosive cladding, the values of the collision velocity and collision angle are time-variant. But they are constant in EXW.

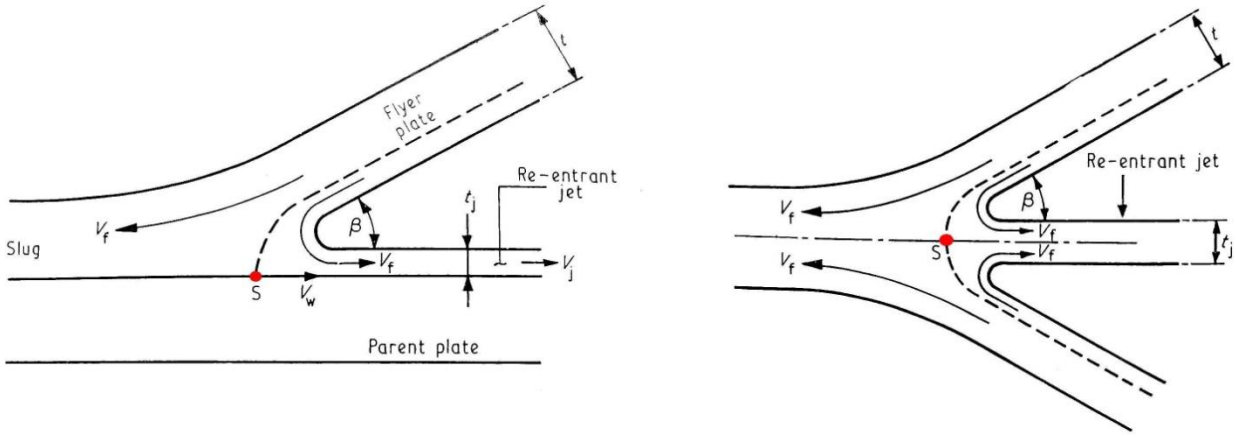


Figure 2.2: Stationary reference frame about the collision point, asymmetric and symmetric [8].

The surface layers of the metals, containing films of contaminants or an oxide layer that are detrimental to establishing a metallurgical bond are swept away, ejected within the mass of the re-entrant jet. The metal plates themselves, now cleaned of surface contaminants/asperities/non-metallics by the jet action are joined at an internal point under the influence of a very high pressure that is obtained near the collision region. The pressure has to be sufficiently high and for a sufficient length of time to achieve inter-atomic bonds. The velocity of the collision point, $V_C$, governs the time available for bonding.

The high pressure also causes considerable local plastic deformation of the metals in the interface of the bond. The bond is metallurgical in nature and usually as strong as or stronger than the weaker material. The quality of the bond and its appearance is influenced by control of

the process parameters. These include surface preparation, initial stand-off gap (separation distance for acceleration), and those associated with the driving energy source. The selection of parameters is based upon the mechanical properties, density, and shear wave velocity of each component.

### 2.1.2. Interfacial Waves

Waves are frequently found at the interface of impact welded metal. A single fundamental physical theory responsible for producing them is as yet not widely accepted in the literature [9].

Though an applicably acceptable weld can be produced with a straight interface, frequently under typical welding conditions the interface shows well-formed regular waves [10]. These waves are significant as a demonstration of the fluid like properties of the materials under the impact conditions.

Understanding the mechanism responsible for their formation also provides us with insight into the collision region and the bond formation. Since interfacial waves are a unique phenomenon to impact type joints, they are indicative of the joint, and thereby also serve as evidence of an impact joint and its quality.

It is important to note that neither straight nor wavy impact welded bonds show significant trapped original surface material, such as oxide. Only with high enough energy input, via kinetic dissipation, can there be found solidified melt pockets at the tips of waves, and some trapped jet material. The progression of wave morphology as energy input increases was established by K. Keller *et al.* (reported in [11]) on the basis of three characteristic ranges of the collision point velocity starting with bonding: laminar, transition, and turbulent – straight, wavy, and melted interface, respectively.

As impact energy increases, initially there is a straight interface with periodic oblique adiabatic shear lines, then smooth waves develop with no turbulence, and later waves can be observed with fore and aft regions of turbulence.

After the onset of a bond, increasing energy input, that is, dissipation of the kinetic energy of the work pieces against one another, there is a progression of wave morphology as shown in Figure 2.3.

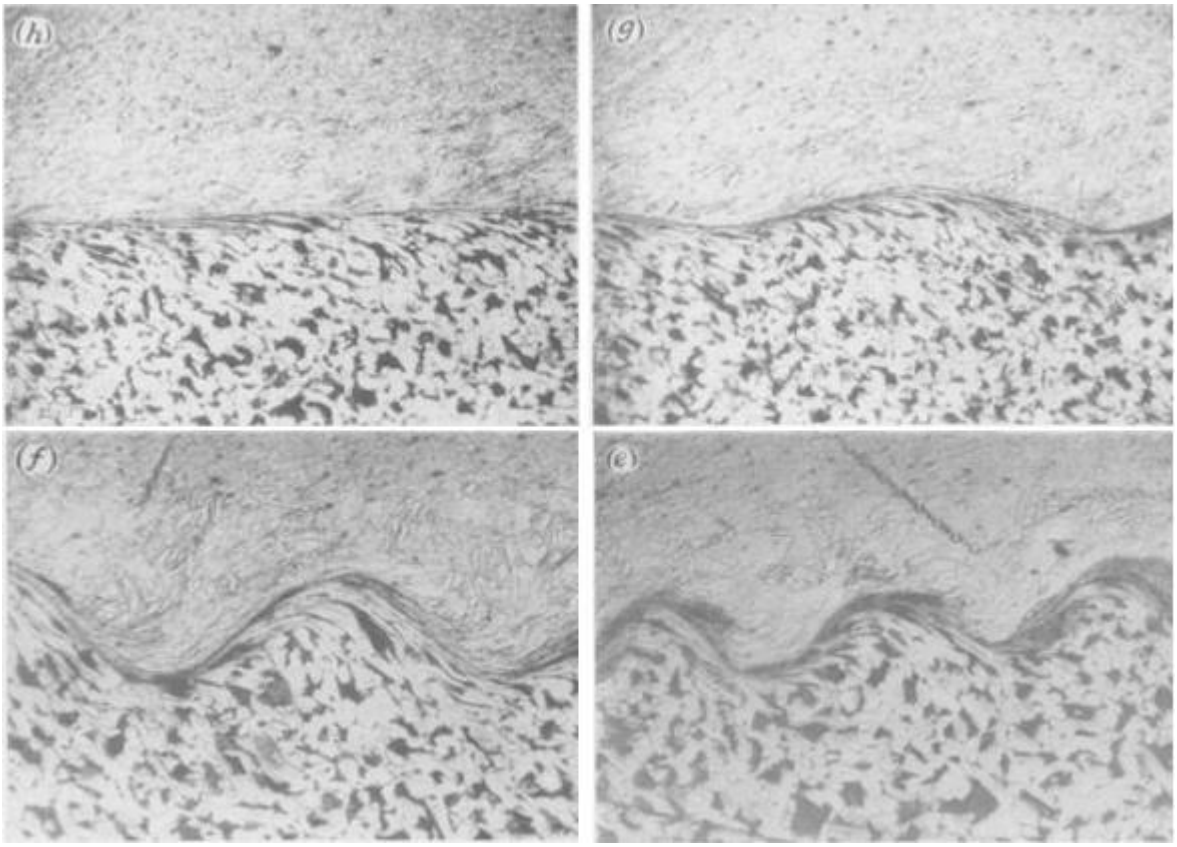


Figure 2.3: progression of wave morphology with increasing impact energy [12].

The presence of jet in the collision region, and the transient fluid-like behaviour under high pressure have led many investigators to seek an explanation and a characterisation of these waves in terms of flow mechanics of one kind or another.

Much like in fluid situations, wave formation begins above a certain, material specific, critical collision point velocity as was found by [13,14]. A Reynolds number can be attributed to this velocity and was found to be ~10 on average with static hardness and density taking the analogue of viscosity in its definition. A useful expression results from this number for the relationship of the wavelength to the impact angle at just above the critical velocity and also as a predictive tool for the onset of waves. It is found that the impact angle has the strongest effect

on the wave size both in length and amplitude, whereas the velocity has little effect on these after the critical point (Figure 2.4).

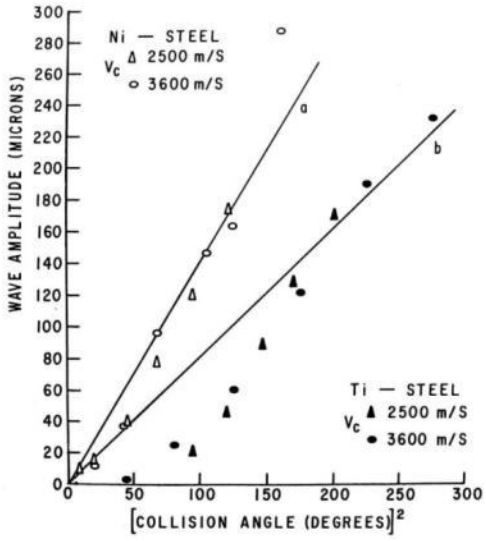


Figure 2.4: Dependence of wave size on impact angle [14]

In the experiments of [14,15] on liquid mediums a hump forming ahead of the collision region was observed. It is speculated that this hump will cause deflection of the re-entrant jet and thereby cause either melting of incoming surfaces or a self sufficient instability to continue through the impact region and also form the waves.

Initially based on the flow-like microstructure of the weld interfaces, the assumption that the metal behaves as an inviscid fluid in the collision region has become the primary one of most investigators; being justified by a negligible ratio of shear stress to applied pressure [12], or very high strain rate [16].

The essence of both the vortex shedding and wake instability, as per [16] is very similar. Each mechanism recognizes the production of the waves as the result of a fluid like instability of impinging oblique streams. Although the arbitrariness of the ‘obstacle’ from which the vortices are shed is superseded, at least conceptually, but the mechanism of [16] in which fluctuation in the velocity profile causes material to shear past itself causing a disturbance and developing into waves just before being frozen by the high viscosity outside the high strain rate region surrounding the collision point. Gordopolov [17] further explains the instability by emphasizing the role of the ‘surface’ tension forces that act to dampen the waves. The ‘surface’

in question here is a thin strip of highly deformed material at the interface that has been speculated based on the experimental observation of a sub-micron thick amorphous layer in transmission electron microscopy (TEM) of cross sections of the interface [1]. It acts much like a flag in the wind; its tension serves to tame the developing waves on it due to the flow of streams on either side. However, the vortex shedding mechanism is known, in fluids, to generate very periodic disturbances, whereas the wake instability is attributed to Kelvin-Helmholtz type flow where periodicity is only present in the first moments of development before becoming a non-linear turbulence. This allows shedding to allow more practical derivations and the development of the Helmholtz type is still in debate about what ceases it (surface tension, increasing viscosity, or other).

### 2.2. Magnetic Pulse Welding

Unlike in explosion cladding, MPW can be either symmetric (double-sided) or asymmetric (single-sided), with deliberate propulsion of either both sheets to be joined or only one, respectively. The asymmetric configuration is typically used for dissimilar material joints because of the different electrical properties of the metals. In this case the less conductive sheet is placed against a die and the other flung at it. In general, the symmetric setup uses the discharge current more efficiently since it accelerates both sheets with it. Also, with this setup higher impact velocity can be achieved.

The MPW technique has been applied successfully to tubes in either expansion or crimping configurations by several researchers. Notably, Dudin [18] and Demichev [19] who applied MPW to nuclear fuel jacket sealing. Also Kojima et al. [20] who measured the magnetic field inside a tubular concentrator and deduced a simplified analytical model for the flow stress of the tube under the compression of the magnetic pulse. However, there is no such symmetry in the sheet configuration and the magnetic field is more difficult to control and locate. Moreover, an analytical model for the plastic bulging behaviour of the sheet is not trivial and is a function of many factors. Some attempts in modeling the bulging have taken place in electromagnetic forming operations (EMF) [21-26]. However, they have yet to be successfully ported to MPW application and there is no particular consensus about which model is most appropriate.

Some of the earliest attempts to join sheet were performed by Aizawa on commercially pure aluminum [27]. Other work has been done since to show that MPW is feasible in joining Al to Steel, Al, Mg, Cu, or Ni [28-33]. These references used mainly single sided MPW with Al as the flyer plate. Currently, most MPW research is focused on joining dissimilar metal combinations, with primary interest in the resulting joint mechanical properties in connection to formation of intermediate phases at the weld interface [28,30,32,34,35]. For example, recently Song *et al.* [36] characterized the steel-Ti dissimilar EXW joint hierarchical structure from macro to nanoscopic level and found mechanical properties to heavily depend on intermetallic formation. However, there exists limited understanding of the connection between microstructural features of similar metal MPW welds and mechanical properties, without the formation of intermetallics. And TEM work of such interfaces, as well as in EXW is recent and limited in extent. Research in MPW between similar metals has been limited to pure Aluminum (Al) or Copper (Cu) or alloys thereof [37-40] because of their high conductivity and consequently ease of propulsion with magnetic fields. No fusion-like features were found in the similar material welds of these studies. Moreover, TEM analysis revealed various peculiarities at the interface including grain refinement to a sub-micron level in Al and Cu welds [41], indicating severe plastic deformation. Mg alloy use in MPW literature has been limited to only being joined with aluminum [30,32]. In these studies primary focus again only had to do with the intermetallic pockets at the interface. Currently, to our best knowledge, no publications in the field report on the feasibility of welding Mg-Mg with MPW or EXW.

The key process parameters in the oblique collision are the collision point velocity and the collision angle which are not independent [42]. In EXW, it is known that after a short initial transient stage, the oblique collision angle (β) at which the sheet surfaces meet and which affects bonding success, remains constant throughout welding [43]. As a result, bonding morphology occurs consistently over a large interfacial area. The welds can be successfully produced when the angle β is within an acceptable range, and its value is chosen by design of the cladding geometry. However, bond morphology in MPW joints is not consistent throughout the joint. This difference was not sufficiently explored in the MPW literature, or in EXW seam welding. It has been suggested by Watanabe *et al.* [40] that MPW's unique weld morphology results from a transient β.

## 2.3. Magnesium Alloys and Severe Plastic Deformation

### 2.3.1. Magnesium

Given the high strain nature of most solid state welding, and especially MPW, it is necessary to examine the plastic deformation behaviour of Mg. Mg has a low ductility ranging about 5-20% and a tendency for anisotropic deformation which can complicate solid state welding. Moreover the texture of rolled magnesium sheets is unfavourable to compression in the normal direction [44] which is the main loading effect of surface to surface impact.

Much of Mg's complex deformation results from its hexagonal close packed crystal (HCP) structure. The primary slip plane of Mg is {0001} (or {0002}). It is shown with the easy slip directions in Figure 2.5 along with the standard HCP directions convention.

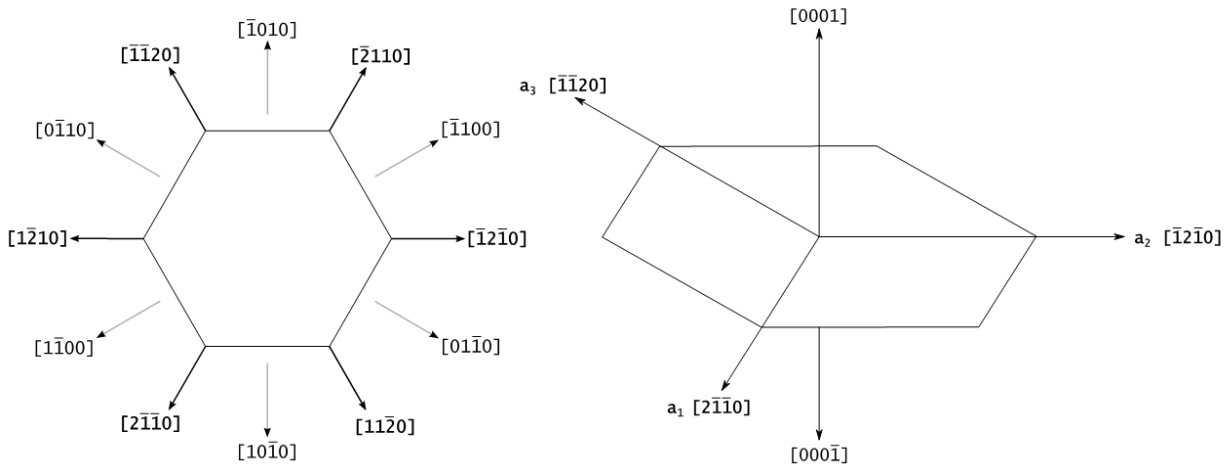


Figure 2.5: Left, slip direction of the HCP basal plane with easily slip direction in bold. Right, HCP convention directions.

Mg slip planes, excluding the basal plane, are shown in Figure 2.8. Deformation by slip in Mg can take place along the easy slip directions above in the basal, prismatic {10-10}, and pyramidal {10-11} planes. <c+a> (not orthogonal to lattice axes) slip has been reported to take place on the type 2 second order pyramidal plane {11-22} [45], and was confirmed by Obara *et al.* particularly in single crystal c-axis compression [46]. Deformation is also largely accommodated by twinning mainly on the {10-12} (tensile) and {10-11} (compressive) planes. Double twinning can also occur with a {10-13} habit [47] and twinning has also been observed on {30-34} [48]. Annealing twins in Mg are not common. Figure 2.6 shows the types of

loading that are favourable to which type of twinning. For {10-12} twinning, compression along the c-axis or parallel to the basal plane is favourable.

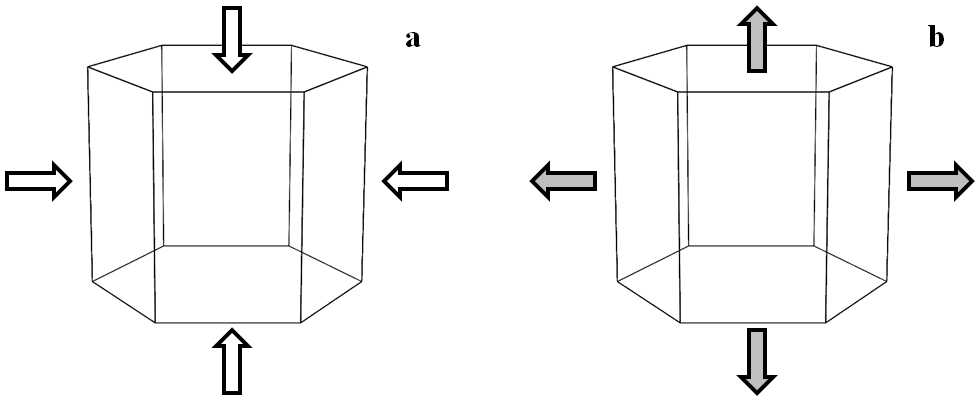


Figure 2.6: Load states that are (a) favourable to {10-12} tensile (expansion) twinning and (b) Favourable to {10-11} compressive (contraction) twinning.

Critical resolved shear stresses (CRSS) values for these different slip systems are widely varied [49], however the general consensus is that $CRSS_{basal} < CRSS_{twinning} < CRSS_{prismatic} \leq CRSS_{pyramidal.}$ The approximate ratio of CRSS values provided by Gehrmann *et al.* [50] for single crystals of 1:T:38:50 (respective to previous order, T undetermined) gives a good feel of how much more preferred basal slip is to the other systems. This ratio, however, may be significantly lower for polycrystalline Mg [51]. The CRSS of both the basal and {10-12} twinning is strain rate independent but that for twinning is also temperature independent [49]. At higher temperatures, typically >225°C ductility is greatly increased by the activation of pyramidal slip on {10-11}<11-20> and/or {10-12}<11-20>. It can also occur at room temperature but at a load direction relative to the easy slip direction as shown in Figure 2.7.

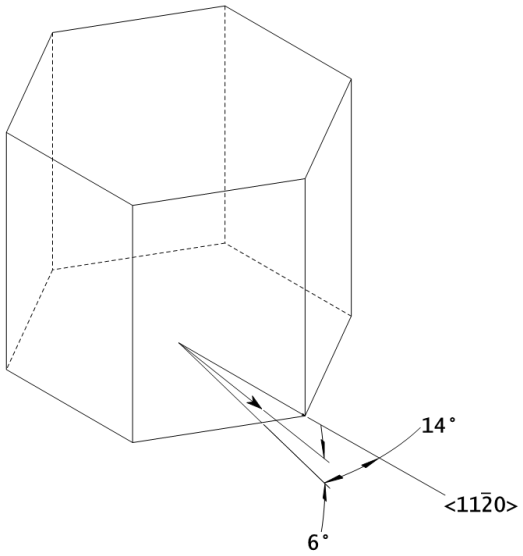


Figure 2.7: Loading direction to activate pyramidal slip at room temperature.

In rolling of Mg sheet the load is almost parallel to the c-axis, resembling Figure 2.6a, and this causes twinning and double twinning to take place [52]. This forms local regions that are favourably aligned for basal slip which can cause high local strain with further deformation, creating shear bands [53,54]. Such shear bands which result from this loading direction are observed at a 45° (±20°) incline to the sheet surface when viewed in cross section.

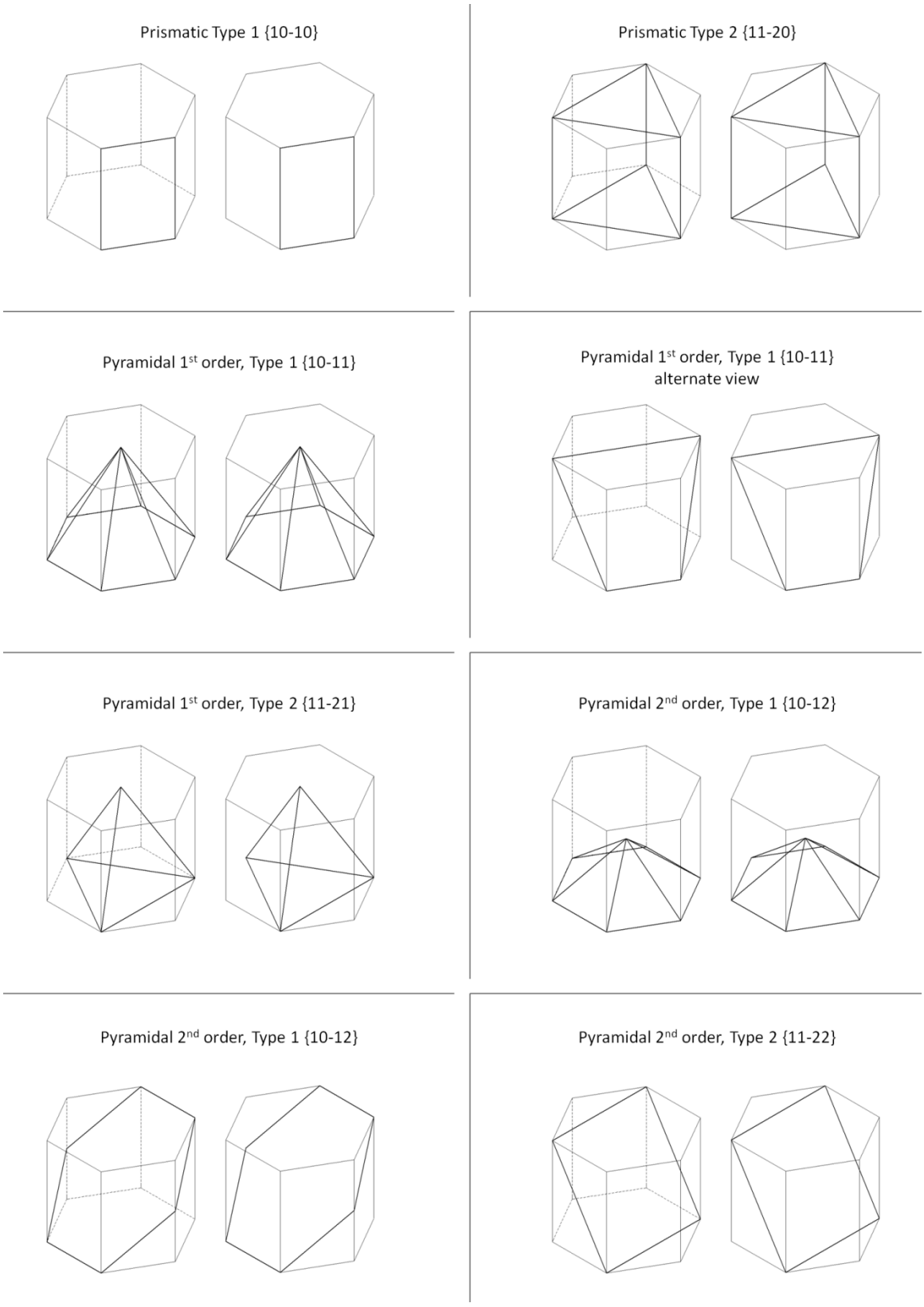


Figure 2.8: Slip and twinning planes of the HCP crystal structure not including the basal plane.

### 2.3.2. Severe Plastic Deformation and Dynamic Recrystallization

In impact welding the strain at the interface can be very high. Using the interfacial waves it is possible to make a conservative estimate of the increase in length of the interface, which has been measured at 150% [7]. Other studies indicate that the re-entrant jet material itself, upon particulation and ejection forwards, undergoes a strain of 600 [55]. The high plastic strain at the interface is made possible by the extreme isostatic pressure that surrounds the collision point, which is several times higher than the material yield strength [1]. These large strains are believed to be accommodated by solid-state flow, by grain boundary sliding and gliding [56]. Grain boundary sliding, especially at high strain rates, occurs after grains have been refined to a sub-micron level via Dynamic Recrystallization (DRX). The mechanism by which the ultra-fine equiaxed DRX grains form is shown in Figure 2.9 and is called rotational DRX mechanism. In applied strain, at first the dislocations align themselves in to a cell network. As more dislocations are generated and move into the cells sufficient dislocation density there forms a grain boundary. The cells become elongated grains which further break up into approximately equiaxed nanograins.

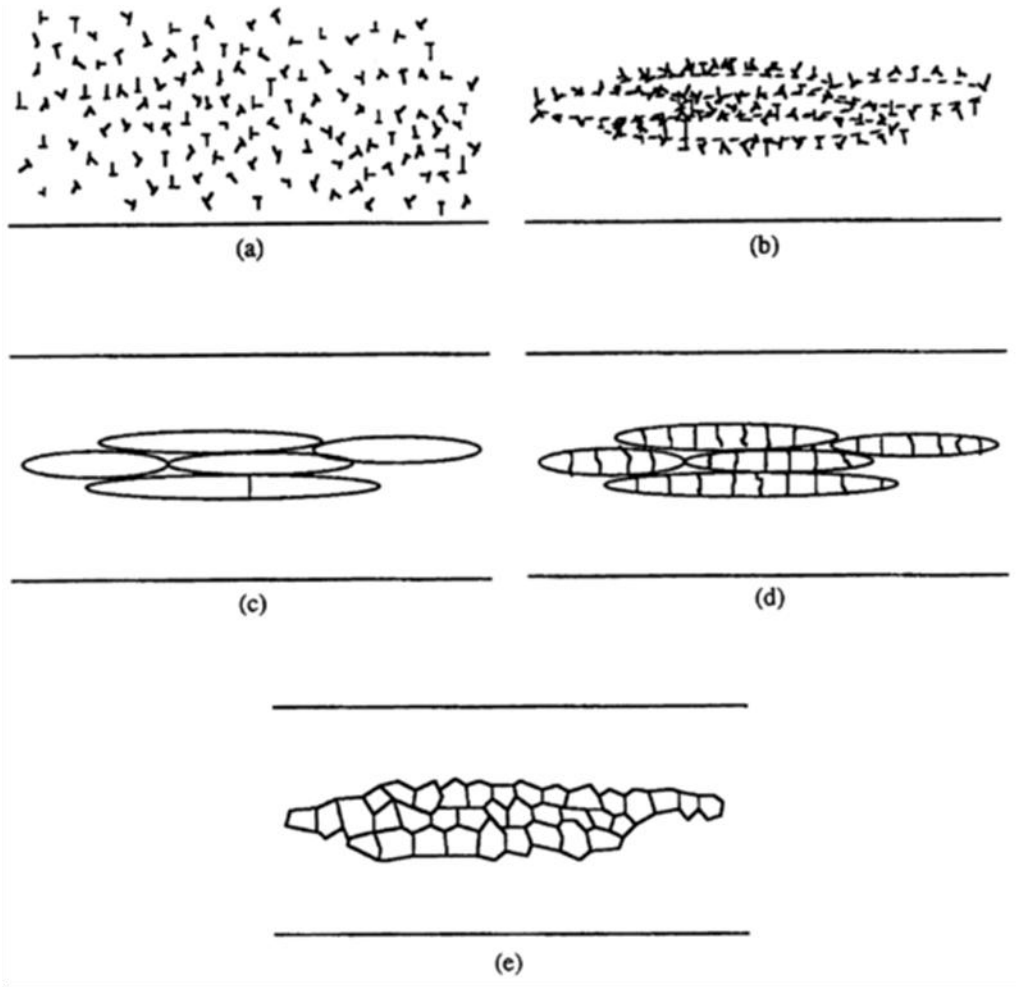


Figure 2.9: Microstructural evolution during high-strain-rate deformation. (a) Random dislocations; (b) Dynamic recovery: elongated dislocation cells form; (c) Elongated subgrains form; (d) Break-up subgrains; and (e) Recrystallized structure (from Meyers *et al.* [57]).

## 2.4. Summary

Impact welding is enabled through the oblique collision whose success is governed by the collision angle parameter; β. β has a weldability domain that depends on many factors including the material itself. Jetting and thus bonding can only occur when β is within its domain.

With regards to the interfacial waves, it seems that the formation of the interface waves is likely a complex competition of processes having to do with mostly shear flow instability and instability of the high energy re-entrant jet. However, it is still an open discussion in EXW

theoretical literature. Also, the preferred impact welded interface should contain waves as a safety against being near the lower limit of bonding where a straight interface occurs.

Magnetic pulse welding literature is very focused, just like EXW literature, around dissimilar joining and detailed investigation of interfacial secondary phases. This is leads to a gap in the correlation of microstructure to mechanical properties. Moreover, there is limited discussion of the morphology of the MPW joint and how it is created.

Plastic deformation of Mg is complex because of its HCP crystal structure which is heavily biased for basal slip and twinning. Moreover, the formation of shear bands reduces ductility due to strain becoming concentrated in these bands and the texture of rolled Mg sheet is highly susceptible to failure in normal direction compression. However, if deformation at the weld interface can raise temperatures high enough then via activation of the pyramidal slip there should be sufficient ductility to endure bonding. DRX is the mechanism responsible for enabling the solid state flow required for jetting and bonding under impact. Given the high strain and strain rate nature of MPW, DRX microstructure can be expected at the interface as it has been found in EXW.

# Chapter 3: Experimental Apparatus and Methods

This chapter describes the material and equipment used to produce and analyze magnetic pulse welds. The various materials used are described along with the respective sample preparation procedure. The welding apparatuses are presented with concise descriptions of their design. Lastly the experimental methods and the numerous metallurgical analysis tools used are described.

## 3.1. Materials

In The current study three different kinds of materials were used, Magnesium AZ31 alloys from Posco and GM, and the third is high purity Mg sheet from Magnesium Elektron. The chemical composition as provided by the respective manufacturers at the time of writing is listed in Table 1 and compared to the American Society for Metals (ASM International) standard composition. Posco sheets are twin roll cast in a 0.6mm thickness. For the AZ31 from GM the thickness of these sheets is 1.6 and 2 mm and the tolerance of the composition was not given by GM. AZ31 from both sources was received in the H24 condition which is the strained partially annealed condition. The effect of joining Mg-Mg with an interlayer was also investigated. A 0.127 mm (0.005") pure aluminum foil was used. Its composition is also provided below.

Table 1: Chemical Composition of Various Materials Used in This Work in Wt.%.

| | Al | Zn | Mn | Si | Cu | Ni | Fe | Mg |
|---|---|---|---|---|---|---|---|---|
| ASM AZ31B | 3.0 | 1.0 | 0.2 | -- Others: 1.0 -- | | | | Bal. |
| AZ31 POSCO | 2.9-2.95 | 0.85-0.95 | ~0.3 | 0.02-0.03 | <0.002 | <0.003 | <0.003 | Bal. |
| AZ31 GM | 2.92 | 1.09 | 0.3 | 0.01 | - | - | - | Bal. |
| Pure Mg | 0.06 | 0.01 | 0.01 | 0.02 | - | - | - | Bal. |
| AA1100-O Foil | Bal. | - | - | - | 0.12 | - | - | - |

Figure 3.1 shows the as-received microstructure of the Posco Mg sheet in the sectioned such that the transverse direction is into the page. This base metal microstructure has equiaxed grains with a bi-modal size in the ranges 6-8 μm and 15-25 μm as measured by average line intercept method from the optical micrograph.

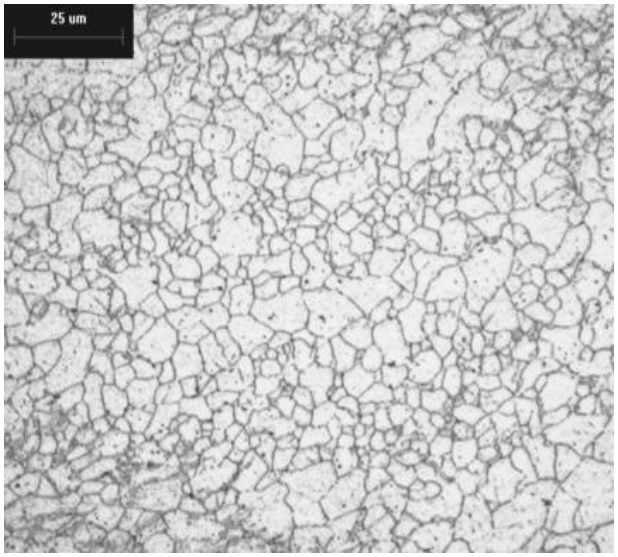


Figure 3.1: Posco supplied AZ31B Mg alloy as-received microstructure.

## 3.2. Sample preparation

For welding of Mg to Al sheets, samples were cut to a length of 120 mm with varying widths from 40-80 mm in 10 mm increments. The Mg sheet was placed as the parent with the aluminum sheet being the one that was propelled at it. To set the standoff gap, the sheets were put together with two 20 mm long strips of double-sided 3.175 mm (0.125") thick foam tape from McMaster Carr (P/N 7626A253). Two pieces of tape were placed flush on the short sides of the sample up to 8 mm from the edge. The samples were then glued together using the tape with the aid of a machinist's square to make certain of their relative alignment. Because of the sprung compressibility of the tape, it serves to press the sheets up against the coils as well as fine tunes the standoff gap using the screw-adjuster of the welding setup. The pure Mg sheet was originally supplied in 1.5mm then samples having thickness of 0.6 mm or 0.7 mm were produced using fly-cutter machining or hot rolling at 375°C

The majority of welding experiments were done using rectangular specimens of 90 mm × 40 mm × 0.6 mm having the 90 mm edge oriented parallel to their rolling direction made from the

Posco AZ31B sheet. Prior to welding, these specimens were degreased by wiping with acetone as the only surface preparation. They were prepared with foam tape in the same way as described above. When an Al interlayer was used, it was attached flush to one of the Mg sheets using a single 10 mm strip of spray adhesive from the upper edge. The foam tape was then placed on it.

## 3.3. Experimental Equipment

The strong pulsed magnetic fields in MPW are generated by the passage of a high amplitude and high frequency current through a narrow conductor. A capacitive discharge is used to produce this current. The conductor itself is positioned in proximity to the welding specimen that is to be propelled by the magnetic fields. This section presents the capacitor machine used and then the coil setup.

### 3.3.1. Capacitor Bank Machine

Two Pulsar MPW capacitor bank machines were used for making welds. They were an 'MPW-20 Research Edition' unit located at the University of Waterloo and a custom 'MPW-100' unit offsite at the Magna Promatek R&D centre in Brampton, Ontario. Figure 3.2 shows the MPW-20 machine cage. The power supply is on the left and the capacitor bank is on the right. The MPW-20 machine is theoretically capable of peak 20 kJ discharge energy. However, the manufacturer has recommended against charging the bank above 7 kV (13.2 kJ) for simple low-inductance discharge circuits. Damage to the capacitor can be caused by a second negative current peak that is more than 60% in amplitude of the first discharge peak. However, the MPW-100 machine is capable of safely producing up to 100 kJ discharge energy. The highest discharge frequency possible with either machine is 21 kHz or 55 kHz, respectively, in short circuit. The MPW-100 machine was used to attempt to increase the skin effect of the induced currents because of its higher frequency.


Figure 3.2: Pulsar MPW-20 Magnetic pulse welding machine at the University of Waterloo.

Both machines, MPW-20 and MPW-100, operate based on the simplified circuit shown in Figure 3.3 and consist of a capacitor bank, high-voltage charging power supply, a spark gap high-voltage switch, and discharge circuit connected to the coils. To operate the machine a charge voltage is set at the control station. The power supply then charges the capacitors up to this voltage at which point the spark gap switch releases the charge through to the large copper busses on the front of the unit. The discharge circuit is connected to these busses and can be any type of coil. The current passes through the coils and is then grounded through the negative bus of the machine. The discharge waveform produced is a rapidly attenuating sinusoidal alternative current.

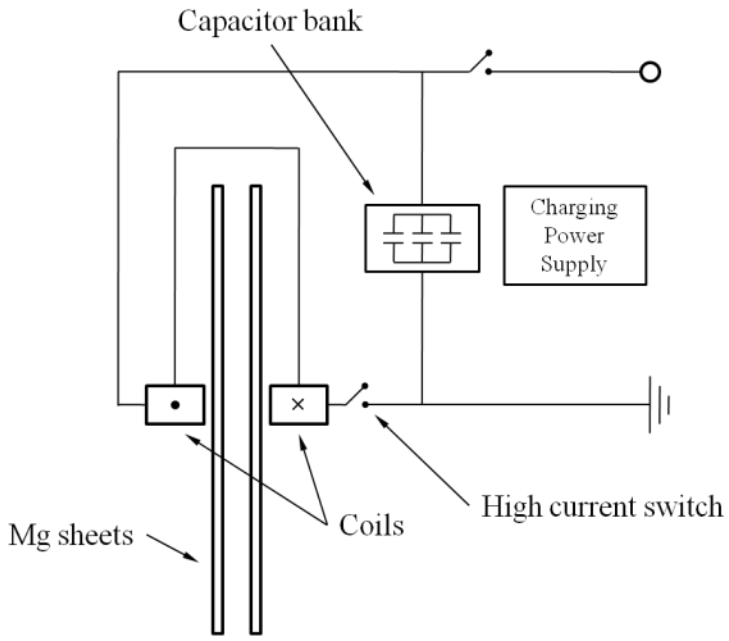


Figure 3.3: Simplified circuit diagram of MPW machine and welding coils

The capacitance is 539 μF and 320 μF, for the MPW-20 and MPW-100 machines, respectively. Operation instructions for the MPW-20 machine are found in Appendix A: Machine Operation.

### 3.3.2. Welding Coil Design

In this work Mg-Al and Mg-Mg MPW welds were produced. A single sided and double sided coils were fabricated for the dissimilar and similar welds, respectively. These designs are briefly outlined in the following subsections and machine drawings are found in Appendix B: Coil Drawing.

#### *3.3.2.1. Single Sided Coil Design*

In order to produce Mg-Al welds a single sided coil setup was manufactured. The setup consists of a single turn, flat, E-shaped copper coil pressed into a machined ABS block (Figure 3.4). The coil and support block were CNC machined at the Engineering Machine Shop of the University of Waterloo. The entire assembly is shown in Figure 3.5. The aluminum sample was placed in front of the coil and the Mg sample was placed flat on the large round die. The single sided design has provision for Hopkinson bar attachment or a crystal force sensor for impact force measurement. Adjustment to standoff gap is made by a large fine thread screw at the back.

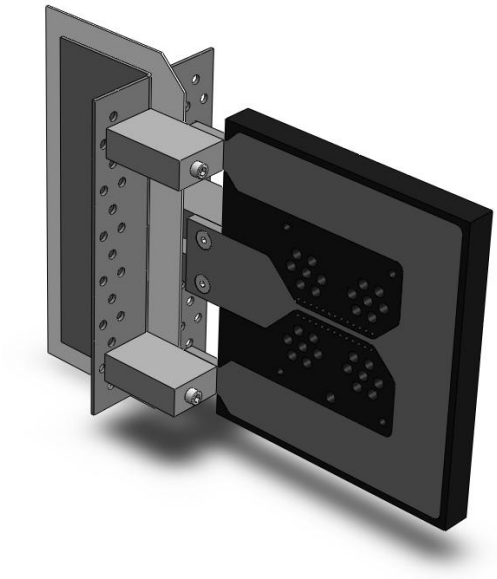

Figure 3.4: View of single sided coil showing basic coil shape with backing and attachment to capacitor bus.

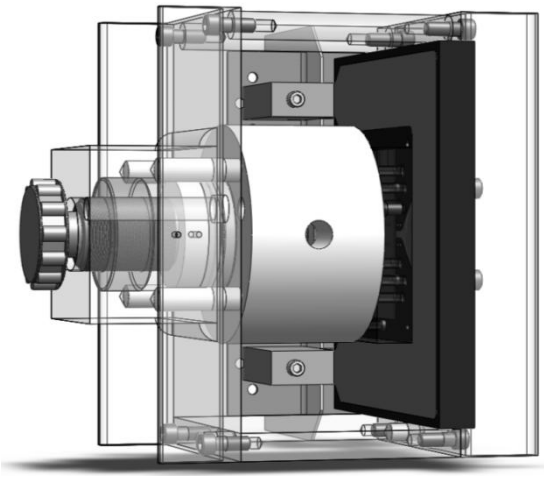

Figure 3.5: Single sided, E-type coil welding setup. Support frame transparent for clarity.

#### *3.3.2.2. Double Sided Coil Design*

In overview, the double-sided design used in this work utilized machined, single turn, flat copper coils in an 'H' shape. The coils were pressed into machined supports of Garolite G-10, which has high strength and impact toughness and is electrically insulating. The flush surface of the pressed coil in the support was insulated by a 0.005" (0.127 mm) thick Kapton® (Polyimide) sheet set down by 3M Super77 spray adhesive. The two facing supports are located together by sprung dowel pins to allow for relative positioning (for adjusting specimen standoff gap). A laminated flexible copper shunt from Spotaloy Products of Ridgetown,

Ontario shorts the coils on one side while allowing motion between them. Figure 3.6 shows the CAD image of this setup with one support hidden for clarity.

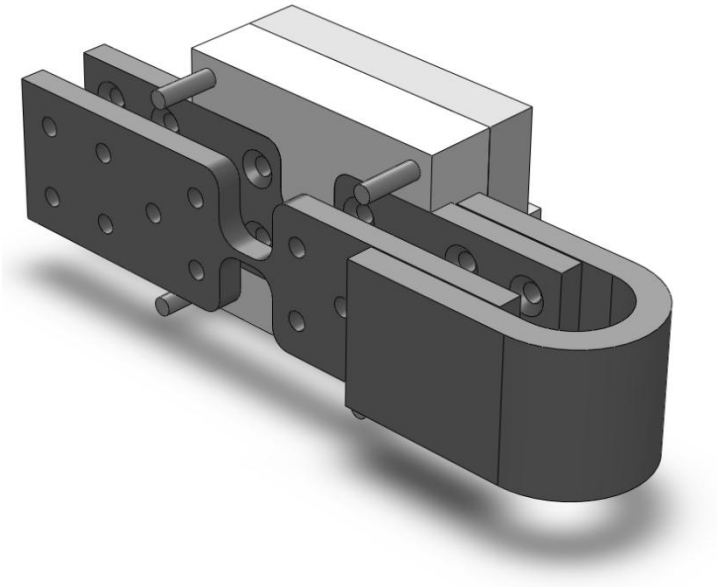

Figure 3.6: CAD image of the double sided coil design featuring H-type coils

### 3.3.3. Welding Setup

Finally, the majority of welds produced were made with a setup of custom symmetric H-shaped copper alloy 110 coils (as in Figure 3.7) connected in a discharge to ground loop to the MPW-20 machine. Each coil concentrated the current through a 9 mm × 7 mm × 3 mm section. The overall length of the concentrator including fillets is 23 mm. The actual weld was formed on the specimens within the area overlapped by the current concentrator. Specimens were positioned with the rolling direction perpendicular to the coil length.

Due to the low electrical conductivity of Mg, 0.8 mm thick commercially pure AA1100 aluminum sheets were used as driver plates and placed between the magnesium sheets and the coils. The higher conductivity of the pure aluminum allowed a larger amount of eddy current to be generated and thus stronger repulsive interaction between it and the coil than in the case of Mg sheet alone.

Figure 3.8 shows a photograph of the completed welding setup as connected to the machine. The coil assembly was mounted in a bench-top vice to allow for standoff gap adjustment.

∅12.7 mm (0.5”) stranded copper grounding cables connect the coil to the machine bus, two pairs per coil.

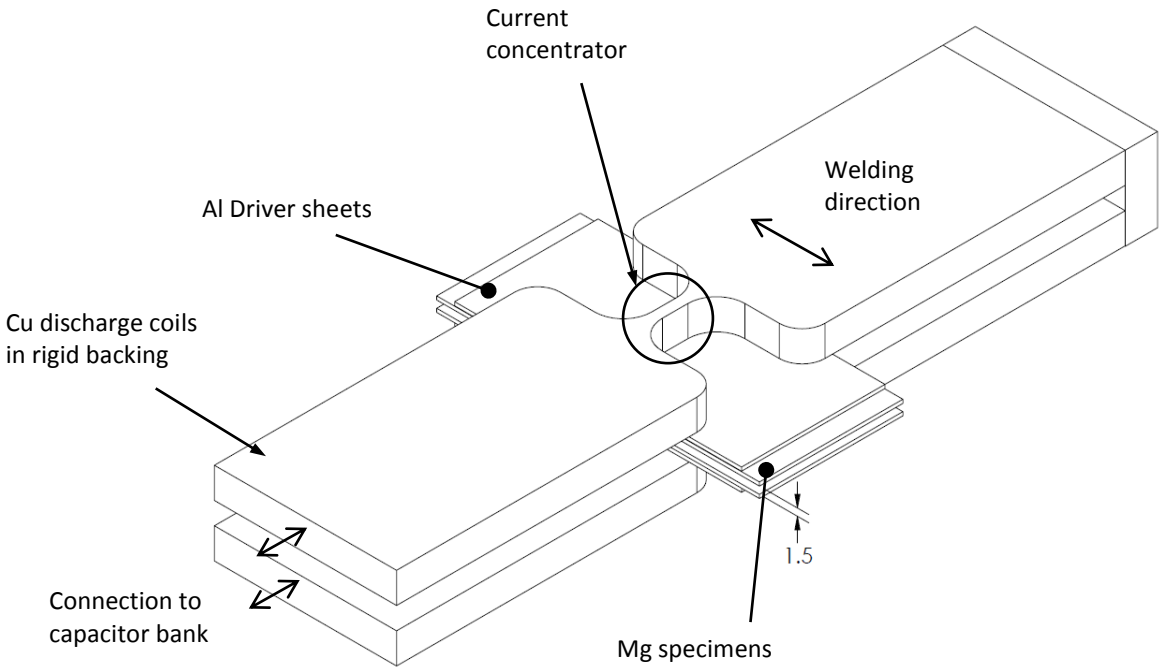


Figure 3.7: Schematic of the final welding setup.

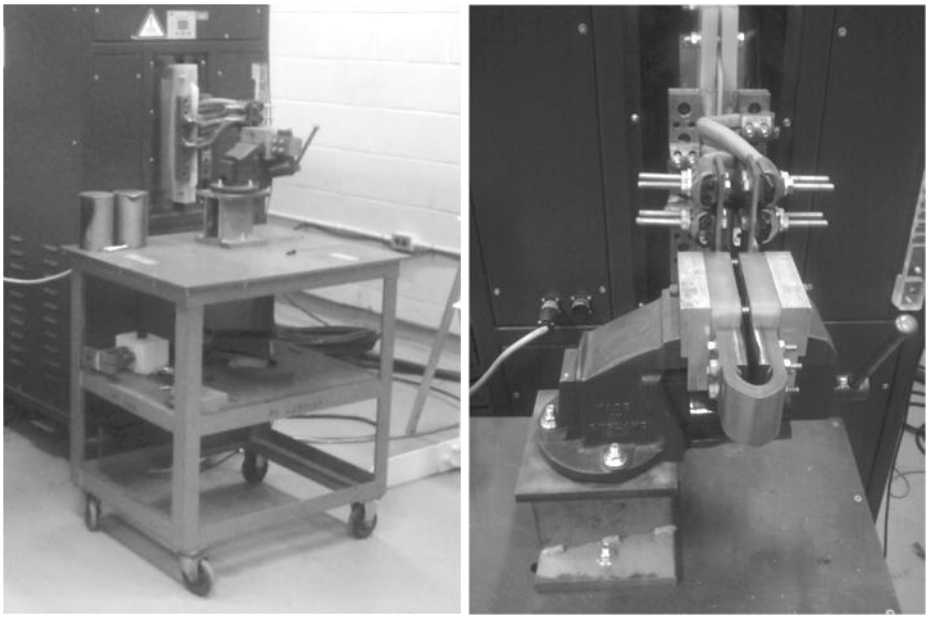

Figure 3.8: Photo of the operating double-sided coil welding setup.

## 3.4. Experimental Method

### 3.4.1. Welding Parameters

Only two welding parameters in the setup are adjustable: capacitor bank charging voltage and the standoff gap distance between the samples. In order to avoid damage to the capacitors the charging voltage did not regularly exceed 6.6 kV. Optimal standoff gap was determined through welds made using 6.3 kV in the range of 0.5 to 3 mm gap. Welds for metallographic analysis were all made at the optimum 1.5 mm gap while varying discharge energy.

### 3.4.2. Data Acquisition

Impact force measurement was not carried out due to what was found to be the extreme high speed at which the collision occurs (see 4.2.2).

An oscilloscope measured and recorded discharge current flow from the capacitors using a Rogowski search coil hooked up around one of the capacitor busses. These curves were primarily used to determine discharge current frequency and peak amperage in order to estimate magnetic driving pressure and skin depth of induced currents.

In initial testing a high speed video camera (Photron Fastcam Ultima APX 120K) was used to observe the sheet motion across the standoff gap. The camera recording was triggered by the oscilloscope upon discharge. Video was taken at 100e3 fps.

### 3.4.1. Jetting Witness

High purity Mg sheet was used to produce welds for which a jetting capture plate was used, called the witness plate. The witness plate was made of Al AA1100. Figure 3.9 shows the witness setup for jetting. These small plates were glued to the foam standoff tape on either of the long ends of the sample.

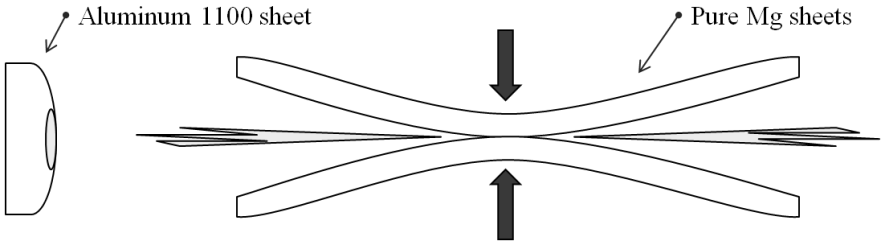


Figure 3.9: Witness plate setup to capture re-entrant jet material.

The witness plate and captured material was examined using a scanning electron microscope (see 3.5.4)

## 3.5. Post Processing

Mg-Mg MPW welds were subjected to metallographic analysis to produce the majority of the results of this thesis. Mechanical properties of the finished joint were measured only using a tensile-shear test to failure and this result was compared with the microstructure.

### 3.5.1. Metallography

All specimens used for metallographic examination were sectioned along the welding direction, cold-mounted, ground, and mechanically polished to 1 μm finish. Grinding sequence was 320, 600, 800, and 1200 coarse using water as lubricant then 1200 fine with ethanol and ultrasonic cleaning in ethanol before and after the last step. Polishing was first done with 3 micron then 1 micron Leco diamond compound on a Struers felt pad at 180 RPM using the oil-based lubricant 'Compound Extender™ 811-003' by Leco. This was followed by finish polishing using Struers OP-S™ 0.04 μm colloidal silica solution (diluted 50% with ethanol) on urethane nap pad at 80-100 RPM. 3 minutes of ultrasonic cleaning submerged in ethanol was done between each polishing step. The specimens were then chemically polished for 5 seconds in 10% Nital solution and etched for 10-30 seconds in a solution of 4.2 g picric acid, 10 ml acetic acid, 70 ml ethanol and 10 ml water.

### 3.5.2. Bonded Area Measurement

After fracture, one half of the joint was scanned in an optical microscope with an automatic computer numeric control stage at 50x magnification. The composite image was visually measured using ImageJ software to determine the size of the oval shaped bond zone. This size was then doubled, with the assumption of the twin bond zones being identical.

### 3.5.3. Hardness measurement

The microhardness of the interface was measured. For microhardness a Vickers indenter machine was used on the etched and polished sample cross section surface. Due to the small size of weld microstructural features a small indentation load was chosen. The resulting small indentation was then measured using an optical microscope at 200x or 500x magnification. To determine the effect of load on the VHN hardness value, several indentations at each load were

made on the as received material. From the results in Figure 3.10, a 10 g load was selected for all subsequent hardness measurements as it had yielded a similar value as 5, 15, and 25 g however its spread was small and the indentation could still be measured with ease via the microscope. The 5 g indentation was too small to be comfortably measured under the microscope, hence its large spread, and so it was not used. Figure 3.11 shows typical indentation appearance and the grid of indentations used.

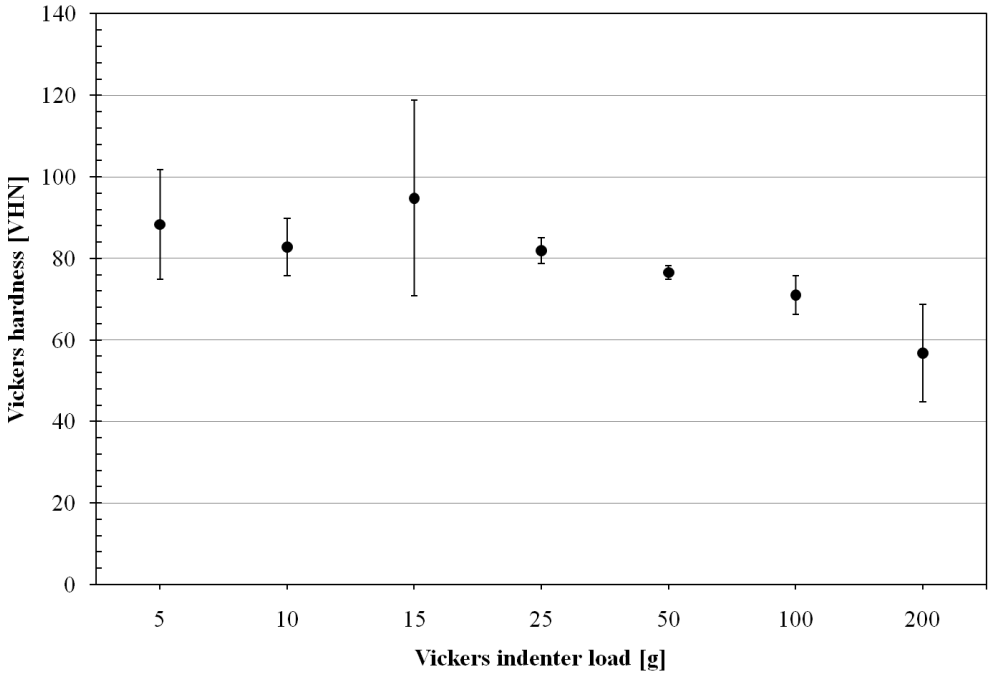


Figure 3.10: investigation into as-received material microhardness using different indenter loads.

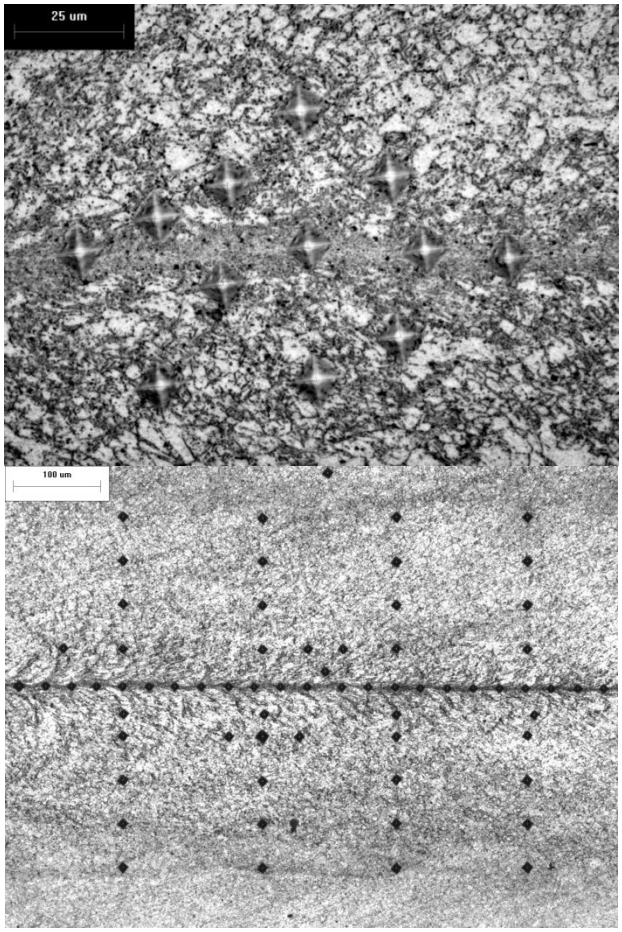


Figure 3.11: Vickers indentations at the weld interface.

### 3.5.4. Scanning Electron Microscopy (SEM)

A scanning electron microscope was used to observe the fracture surface as well as cross section. Samples for SEM were not mounted in cold-mounting resin but rather in an all metal clamp for better conductivity of the electron beam. The clamp was made from 2 mm thick AZ31B (Figure 3.12). Etched cross sections for SEM were deep-etched by immersion in etchant for 3-5 minutes. The welds were examined using a JEOL JSM-6460 scanning electron microscope (SEM) equipped with an Oxford ultra-thin window detector Energy Dispersive Spectrometer (EDS).

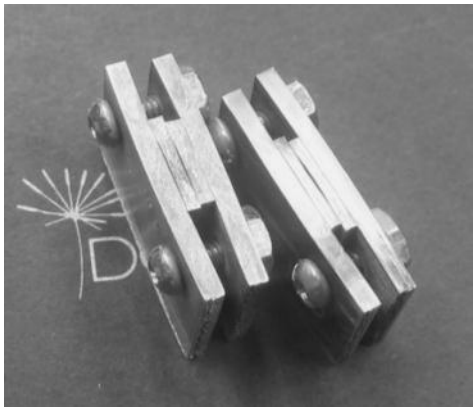

Figure 3.12: All Mg mounting for SEM samples.

### 3.5.5. X-ray Diffraction (XRD)

Micro X-ray analysis was performed on a Rigaku AFC-8 diffractometer with Cu target, 50 kV acceleration voltage and 40mA current after surface grinding to 1200 grit fine. The collimator size used was a 300 μm diameter spot. This spot size covers about half the thickness of the sheet and is good for targeting the bond zone itself. However, for targeting the through thickness microstructure near the bond zone or near another zone a smaller collimator size is better. 100 μm diameter spot was attempted but noise-to-signal was too high to get useful diffraction peaks.

### 3.5.6. Transmission electron microscopy (TEM)

Two methods for TEM observation were carried out. Firstly, thin foils were prepared from 3-mm discs cut on the cross-section of bond zone of welds and then thinned by ion milling process. The welded substructures were observed with a JEOL JEM-3010 transmission electron microscope operated at 300 kV accelerating voltage.

Secondly, to examine the weld interface in detail, Focused Ion Beam (FIB) milling at the University of Western Ontario was used to prepare a thin foil TEM sample. A 35 μm long sample was cut across the bonded interface and captured both bond and nearby microstructures sufficiently. The FIB sample was observed with a Philips CM12 TEM located at the McMaster University in Hamilton, Ontario with accelerating voltage of 120 kV. Figure 3.13 shows the cutting location of the sample on the interface and the prepared sample after extraction with an approximately 10 × 20 μm viewable area.

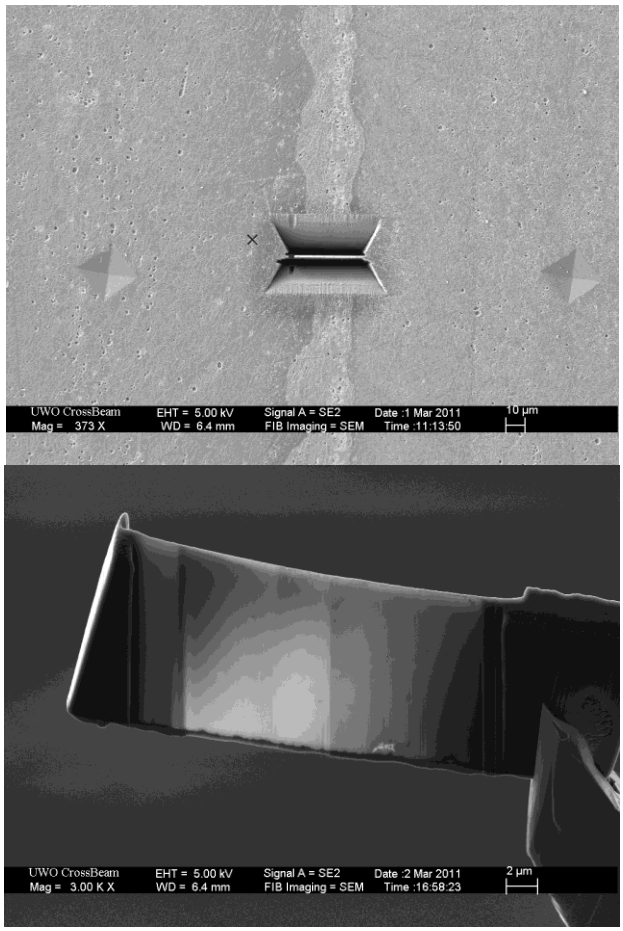


Figure 3.13: Cut location and the prepared and extracted FIB TEM sample.

### 3.5.7. Tensile Testing

The mechanical properties of the welds were assessed through a tensile-shear test until fracture. The machine used was a United 545 with an Instron A532-1, 150 kN load cell in an original Instron 4206 hydraulic frame. The test crosshead rate used was 0.2 mm/min with a break sense of 20%. The sample was preloaded to 2 kg at a rate of 0.1 mm/min prior to the test.

Completed welds were prepared for tensile testing by cutting off one side of each sheet up to 10 mm of the lap bond on opposite ends. The cutting was done carefully as some samples having a weak joint had a tendency to break in rough handling. A vertical band saw or sheet metal shears were used to cut.

Figure 3.14: The United/Instron hydraulic tensile testing machine used in this study.

# Chapter 4: Results

Successful Mg-Mg welds were not possible on the original single-sided e-type coil. This setup was capable only of welding Mg and Al, with Al acting as flyer and Mg sheet as parent (resting on the die). The low conductivity of Mg did not permit sufficient driving pressure to develop when it was used a flyer in the single sided coil setup. Thus Mg-Mg welds could only be achieved when using the double-sided h-type coil design as outlined in 3.3.3.

This chapter first briefly shows the load bearing capacity of welds with and without Al interlayer as well as the fracture surfaces. Thereafter the majority of this chapter presents analysis of Mg-Mg joints made using the double sided coil, in particular of the bond zone microstructure. Metallurgical analysis of these welds consisted of cross section microstructure observation with optical microscope and scanning and electron microscopes. X-ray diffraction was also used to check for secondary phase formation and the texture of the bond zone.

## 4.1. Surface Analysis

As a possible factor in joining, the surface of the 0.6 mm AZ31B material was analyzed using SEM-EDX and Optical Profilometer. For a rough assessment of surface oxide, samples were first cleaned in a solution of chromic acid at time intervals of 15 s up to 90 s and EDX was used to determine oxygen content. The surface roughness against the rolling direction was measured of each cleaned sample using the optical profilometer. Results are outlined in Figure 4.1. It was found that acid cleaning had no apparent effect on the roughness and more than a 15 s acid was unnecessary for surface oxide reduction.

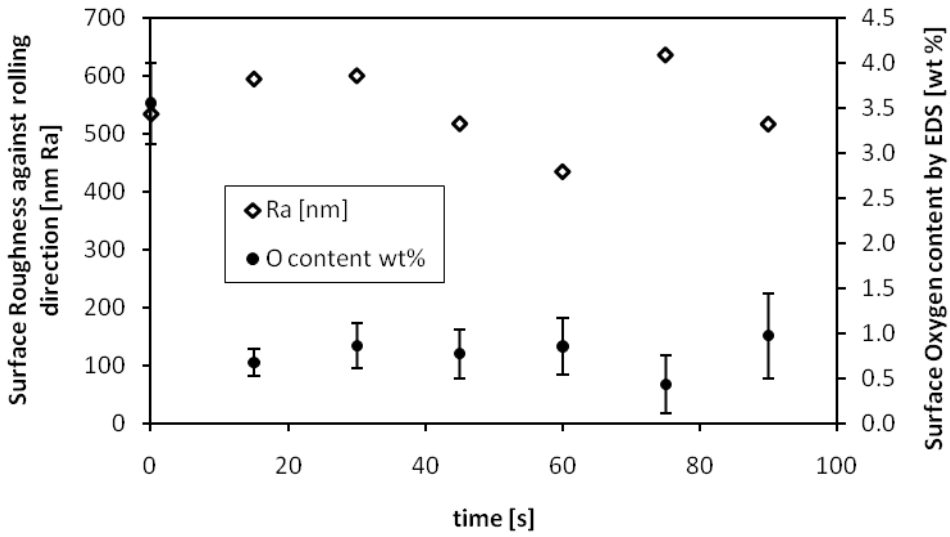


Figure 4.1: Surface oxide and roughness measurements of acid cleaned samples.

Figure 4.2 shows the typical surface of the 0.6 mm Mg sheet as before and after acid dip. The surface roughness average along the rolling direction was measured with a "Taylor-Hobson Surtronic™ 3+" sliding needle instrument at 0.18 μm Ra.

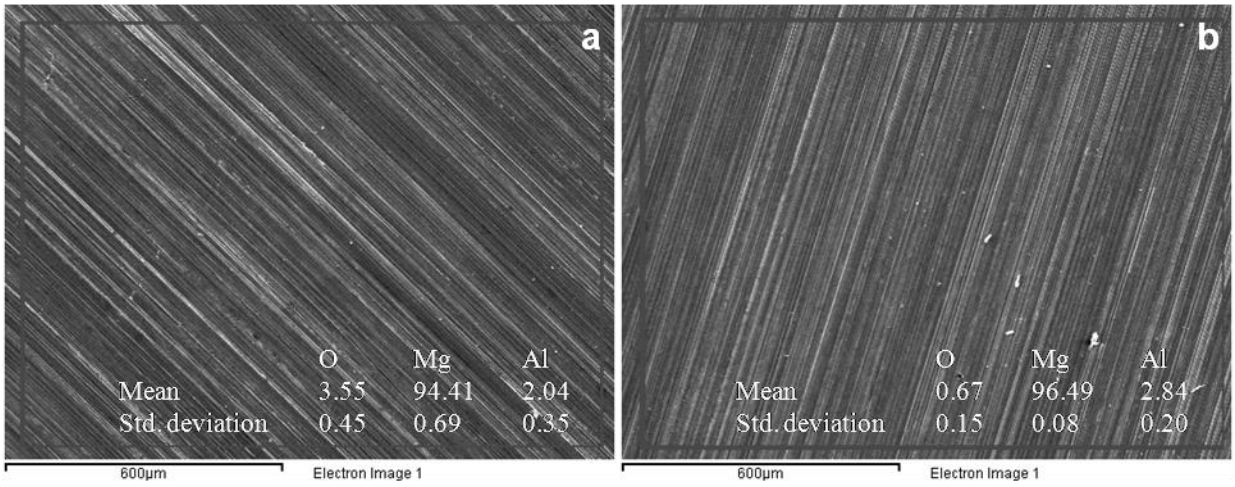


Figure 4.2: SEM image showing the typical as-received surface and the acid cleaned surface of 0.6 mm POSCO AZ31B sheet.

## 4.2. Coil

### 4.2.1. Deterioration

Using Garolite G-10 supports, in conjunction with the MPW-20 bank, the copper coils were able to withstand roughly 50-100 welds before rapidly deteriorating in efficiency of

propelling the sheets. First the square edges of the concentrator slowly become rounded, since they are a high current density area. Then it was found that the concentrator would slowly bend away and the distance between it and the specimen grew, thus causing a reduction in magnetic pressure. A thin, coloured oxide film formed in the area of highest current density on the coil suggesting a significant temperature rise.

An aluminum AA6061-T6 coil of the same geometry was used with the MPW-100 machine at Promatek. This coil failed instantly with the application of a 31.4 kJ discharge. Its appearance afterwards indicates a fuse like failure of the concentrator due to over-current.

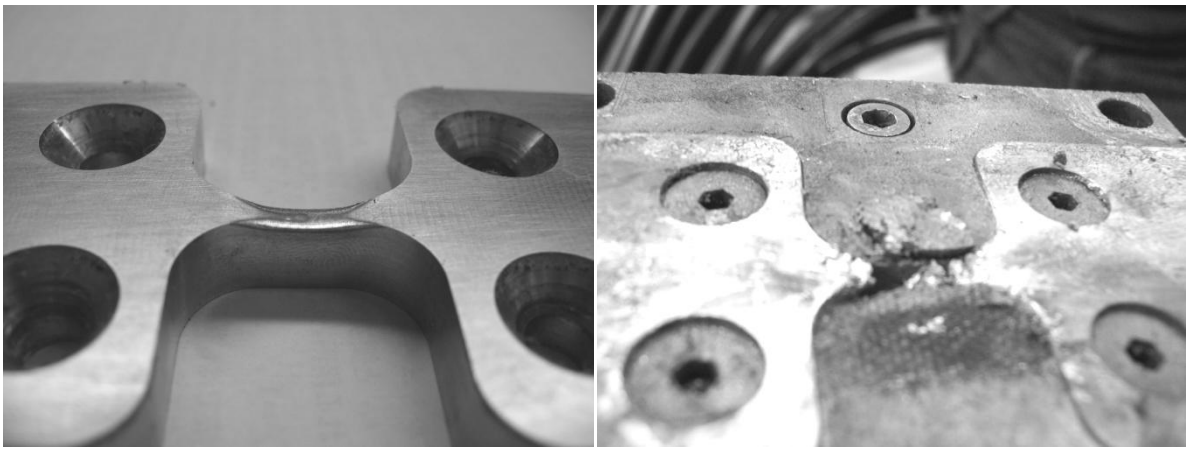

Figure 4.3: Severely damaged coils. Left: bent concentrator in copper coil also showing oxidation caused by heating. Right: aluminum H-type coil after fuse-like failure of the concentrator in application of excessive discharge energy.

Figure 4.4 shows a possible improved design cross section design for the coil concentrator. This geometry was manufactured but the support blocks designed to hold these coils was defective and general welding was not conducted with this design. Time did not permit re-design of the support blocks (see 6.2 Recommendations).

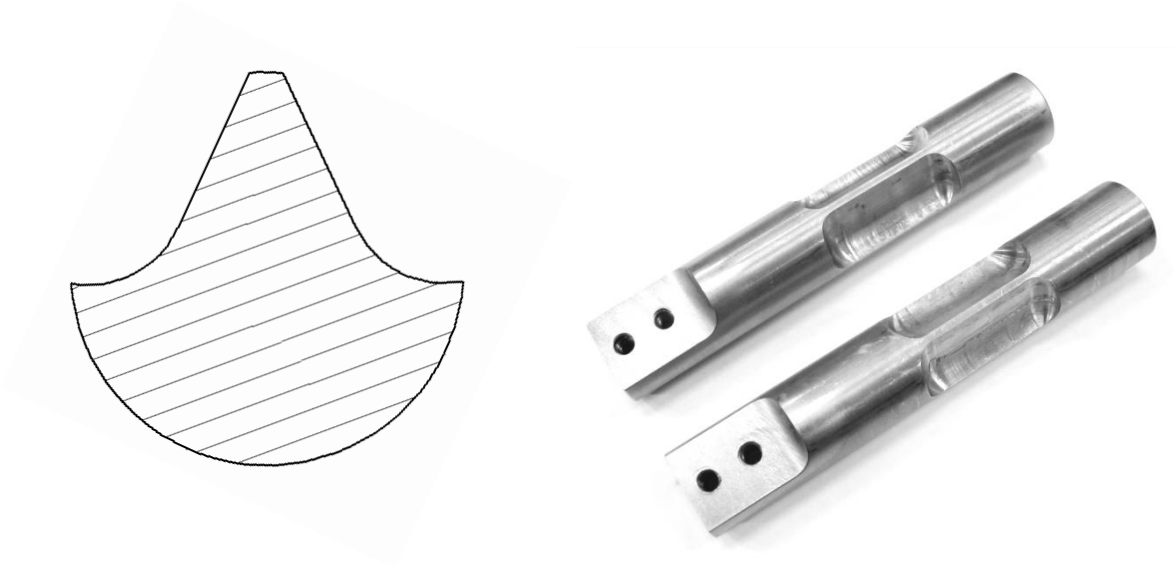

Figure 4.4: Proposed cross section design for a longer life coil and machined prototypes from C110 ∅1” bar.

From electromagnetic die forming experiments at Ford R&D, Golovashchenko [58] noted that the mechanical strength of the coil is not defined by the strength of the material that it is machined from; rather it is mostly dictated by the reinforcement of the coil against observed failure modes, which requires iterative design-testing. This is a valid conclusion for the bending of the copper h-type coil observed in this work. However the fuse like failure of the aluminum coil has to do with its lower conductivity than Cu.

### 4.2.2. Discharge and Weld Duration

Figure 4.5 shows the oscilloscope measured discharge current waveform from an MPW weld made with 6.1 kV charge on the MPW-20 machine. The typical frequency of these sinusoidal rapidly attenuating discharges was approximately 18.5 kHz.

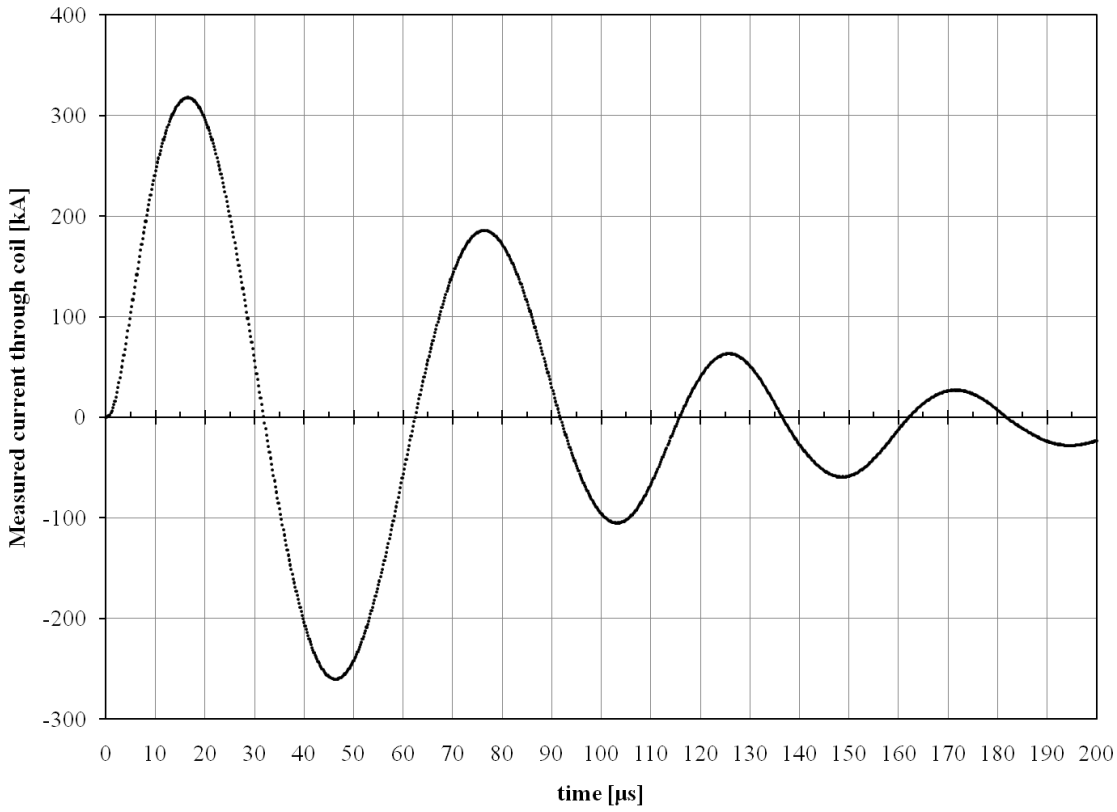


Figure 4.5: The entire discharge waveform of a typical weld.

Using the high speed camera it was found that the entire welding process was apparently complete by the second frame at a 100e3 fps rate. This means that the magnetic pulse weld took less than 10 μs to make. The welding was complete with less than two thirds of the first discharge peak. The rest of the magnetic pressure generated served to only shake the already bonded samples inside the coil setup. The average flight speed of the samples across the standoff gap is therefore on the order of 100-200 m/s. Therefore impact force measurement using a crystal load cell (whose resonant frequency is ~25 MHz) was not possible. Also findings (see 4.3) on the nature of the bonding mechanism and shape of the bond zone made the perpendicular measurement of the impact force using a split Hopkinson bar unnecessary.

## 4.3. Joint Morphology and Formation

Figure 4.6 shows a photomicrograph of a typical cross section of the entire joint in a magnetic pulse weld between two AZ31 Magnesium alloy sheets. Overall, the cross section of the weld is symmetric with respect to a vertical line through the centre of the bonded sample.

The figure also includes a diagram of the relative position of the coil concentrators. The length (into the page) of the impacted area corresponds closely to the length of the concentrator section. The different sections within the width of the impacted area are an unbonded centre zone, two bond zones and two unbonded outer zones. After that there is a drastic bend in the sheet signifying the limit of the material that experienced impact. The unbonded centre zone is approximately as long as the width of the concentrator, in this setup ~3 mm. bonding clearly did not occur along this zone and a rebound gap is visible. On each side of the unbonded centre zone, there are ~1mm long bond zones. The bond zones are symmetrical about the centre line of the coil, having identical appearance. Beyond the bond zones, the specimen sustained impact, but did not join. These two outside regions are about 4 mm long and referred to as the unbonded outer zones. The overall appearance of the impact area is as a crest of a bulge that was flattened (further discussion in Chapter 5:)

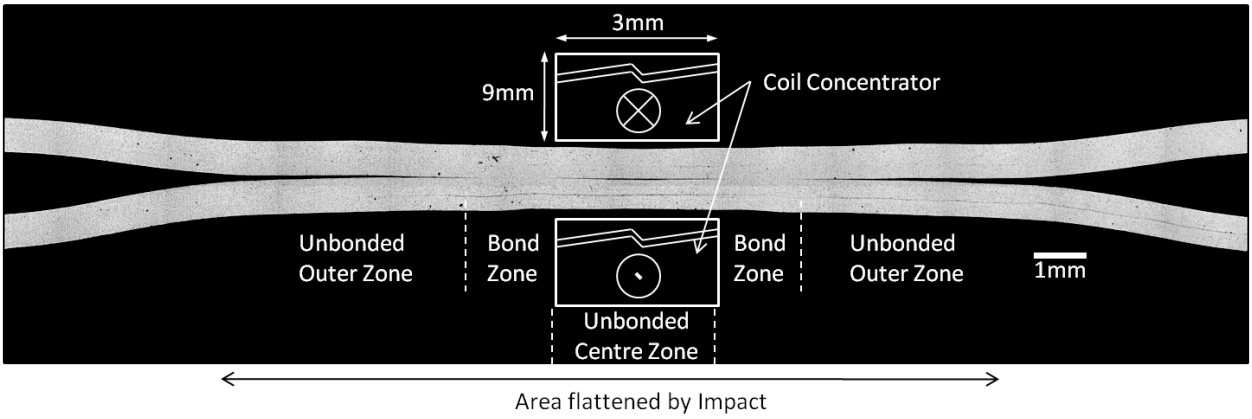


Figure 4.6: Stitched photomicrograph showing the entire cross section of a typical magnetic pulse weld.

Figure 4.7 is a stitched SEM image showing the unbonded centre zone with transition to the bond zone. In the unbonded centre zone, where normal compressive loading through sheet thickness occurred, the oxide layer is still present. Interestingly, in the transition to the bond zone, bonding began to occur intermittently since cleaning of surface contaminates and oxides via jetting started here.

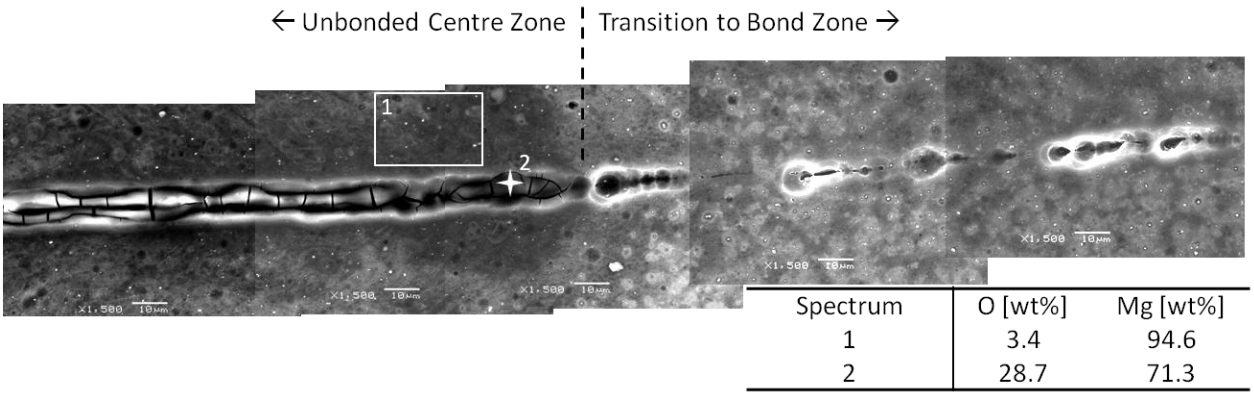


| Spectrum | O [wt%] | Mg [wt%] |
|---|---|---|
| 1 | 3.4 | 94.6 |
| 2 | 28.7 | 71.3 |

Figure 4.7: SEM image showing the unbonded centre zone and the transition toward the bond zone including EDS of the oxide layer.

### 4.3.1. Impacted Area and Fracture Surface Observations

In association with the welding process, there were a number of side effects that were observed on the impacted area after completion of joining. As shown in Figure 4.8a, there was a multitude of small surface cracks found in the unbonded centre zone. These were likely forming due to the brittleness of the alloy sheet when loaded in the normal direction. These cracks did not penetrate the material deeper than 25-40 μm (Figure 4.8b).

With every weld sparking took place between the sheets. The sparks were thought to be a problem in terms of a reduction in the energy efficiency, that is, through grounding of eddy current between the sheets and thus reducing the driving pressure. This reduction in pressure would only occur if the sheets were exchanging sparks while in flight. However, it was observed in the high speed video that white-out due to the sparks occurred only after bonding was complete. Thus the only possible problem with sparking is craters which can be as deep as 100-200 μm like, in Figure 4.8c, and could become stress concentrations. There was no sign of sparks in the unbonded centre zone and bond zones due to them being formed before sparking began.

Figure 4.8d shows a small portion of the dark fracture surface of the bond zone where it meets the unbonded centre zone. A pile up of fracture oxide layer and contaminants is found just before it, completely covering up the rolled surface of the sheet (like that of Figure 4.8a).

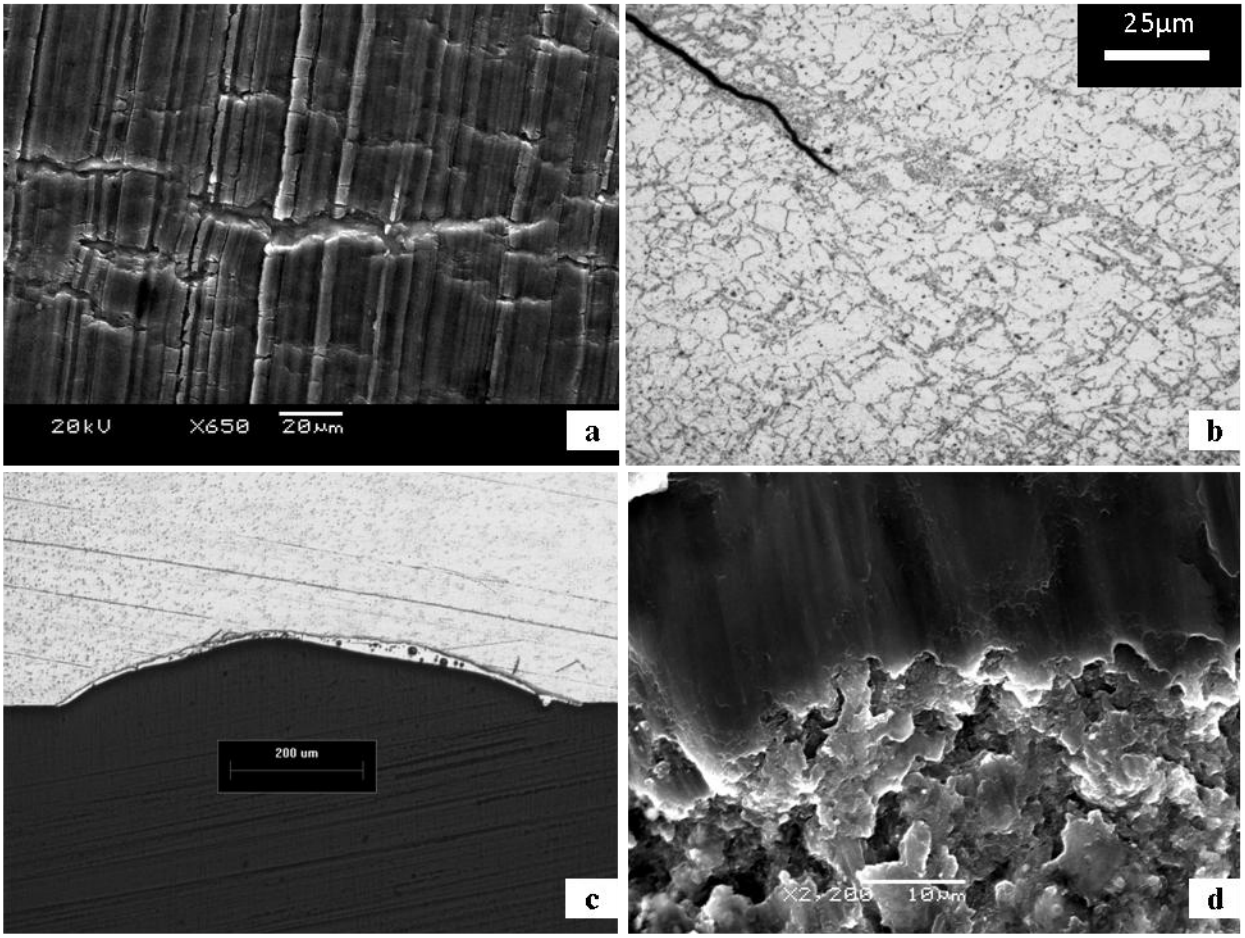


Figure 4.8: (a) crack in the unbonded impacted surface of the Mg sheet. (b) An etched optical image of the cross section of an impact surface crack as those seen in (a). (c) Optical image of the cross section of a spark crater in the vicinity of the bond. (d) Oxide and contaminant pile-up at the start of the fractured bond zone.

The fracture surface of one bond zone of two welds is shown in Figure 4.9. These samples made with discharge energies of 10.2 kJ and 11.6 kJ, respectively. The bonded area of these samples (#8 and #22) was measured at approximately 6.3 $mm^2$ and 9.4 $mm^2$. The corresponding joint shear strength was approximately 140 MPa and 190 MPa, respectively. These numbers are within the typical 100 MPa to 200 MPa shear strength range of AZ31B-H24 magnesium alloy [3]. The bond zones from the fracture surface view are oval in shape. Interestingly, the thickness of the bond zone for both samples is about 1 mm. However, the overall length of samples #8 and #22 are about 3.8 mm and 6.4 mm, respectively. The weld sample #22 carried a higher load to failure as well as had a higher strength however the length of its bond zone in cross section was the same as that of the weaker bond of Figure 4.9.

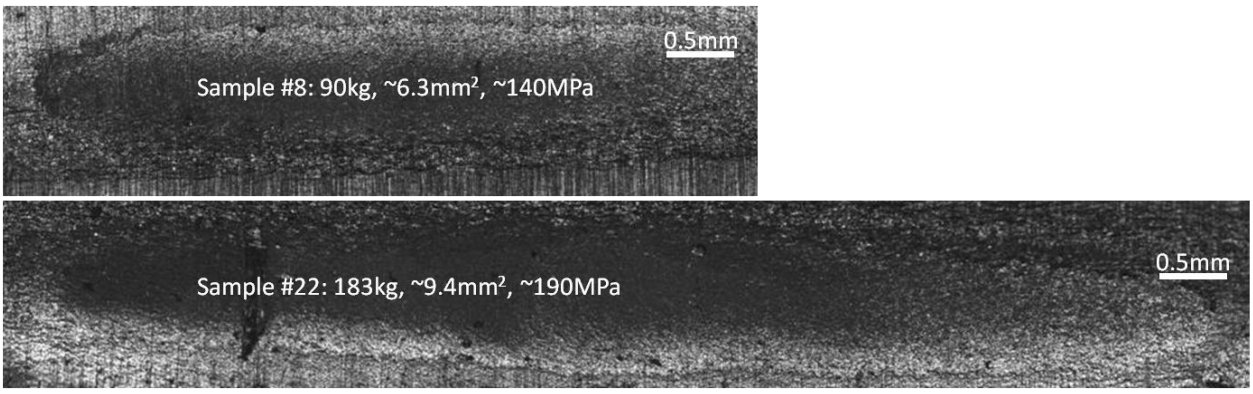


Figure 4.9: Selected sample fracture surfaces showing the size of bonded area.

A closer look at the details of the fracture surface is provided in Figure 4.10. Two distinct fracture types are found along the welding direction, at the beginning and in the latter half. A fine micro-void, ductile fracture surface (Figure 4.10b) appears at the end of the bond while a straight interface at the beginning of the bond zone shows a more brittle fracture surface with large platelet-like features (Figure 4.10c).

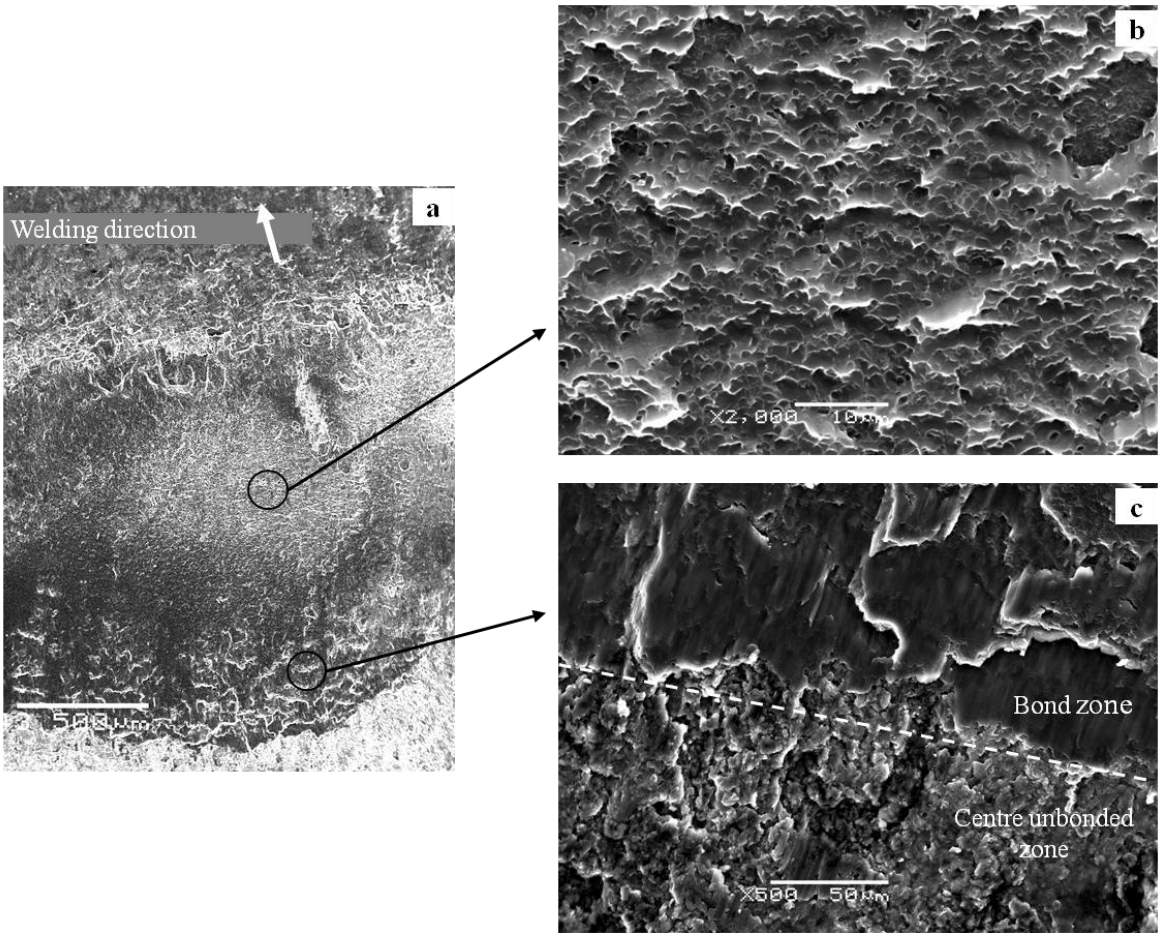


Figure 4.10: a) Fracture surface overview, b) brittle fracture, c) ductile fracture.

### 4.3.2. Re-entrant Jet Witness

The pure aluminum jetting witness plate was viewed in the SEM. Dark splashes of pure magnesium and its oxide were found on the surface. The result and EDS analysis is provided in Figure 4.11. The shape of the mg splash on the plate indicates a liquid or semi-liquid impact with it.

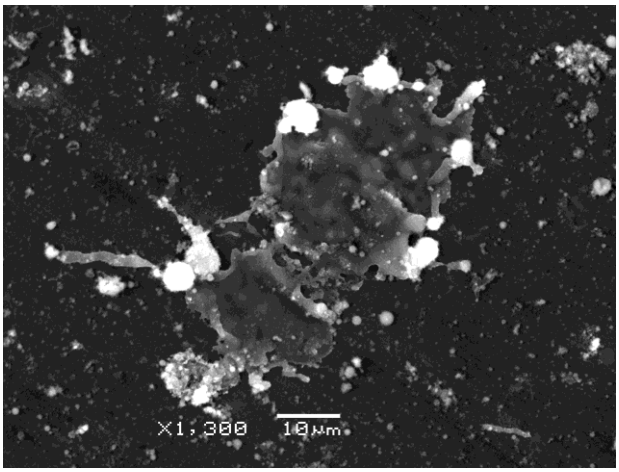


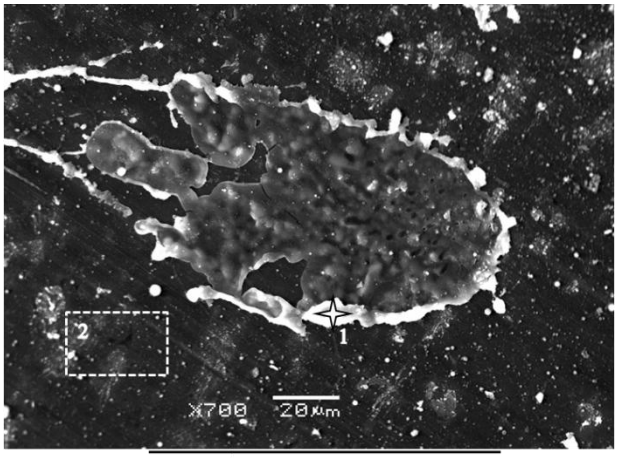


| wt% | O | Mg | Al |
|---|---|---|---|
| #1 | 8.9 | 84.0 | 7.1 |
| #2 | 5.5 | 2.6 | 91.9 |

Figure 4.11: Jetting witness plate showing jet splash and EDS result.

## 4.4. Mechanical Properties

### 4.4.1. Mg-Mg MPW Welds with Al interlayer

Thin pure aluminum foil (see 3.1 and Table 1) was used to facilitate bonding between Mg sheets because originally the efficiency of the welding coil setup was low to the point that the capacitor bank was not providing sufficient discharge energy. A softer material at the interface was sought to improve deformation and thus cleaning. Figure 4.12 compares the load bearing capacity of MPW welds made using an Al interlayer and those without. Welds made with the Al interlayer have a higher breaking load in tensile shear in general over those without

interlayer at any specific discharge energy (charge voltage). Cross section images of the bond zone of these welds can be found in 4.5.3.

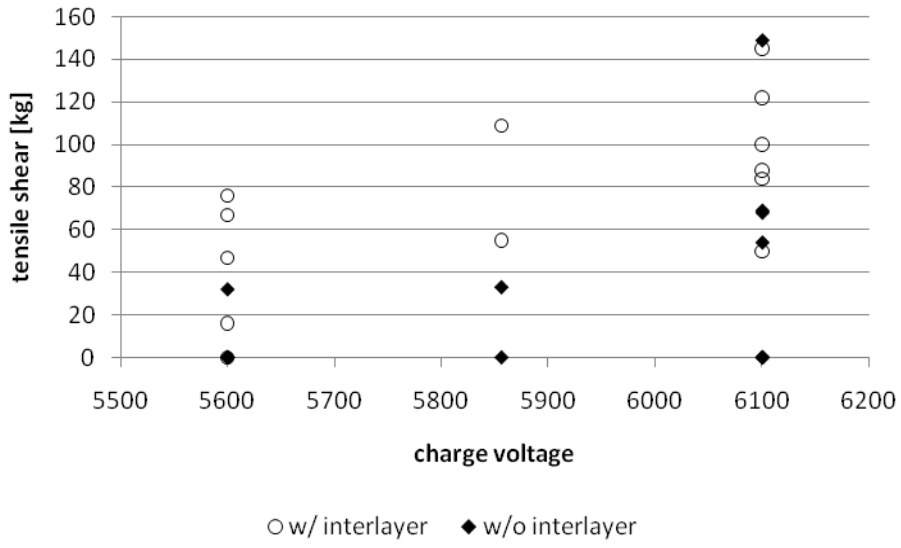


Figure 4.12: Load bearing comparison of Mg-Mg welds made with and without a thin Al interlayer.

### 4.4.2. Mg-Mg MPW Welds

Utilizing the improved welding setup described in 3.3.3, 36 Mg-Mg welds for analysis were produced without Al interlayer using 9.7 kJ – 12.1 kJ of capacitor discharge energy with the standoff distance held at 1.5 mm. The experiment consisted of 6 increments in discharge energy having 6 samples each in a fully randomized order. The resulting lap joints were tensile shear-tested. Breaking load was plotted against the discharge energy as shown in Figure 4.13. Considerable scatter in the data is presumed to be due to the use of the aluminum driver sheets which reduce the consistency of sample preparation. The breaking loads generally increased with the discharge energy as seen from the averages of each discharge energy group. In Figure 4.13, a transition at approximately 11 kJ takes place below which the strength of the welds remains relatively constant and afterwards shows an increasing trend. The strength was determined for representative samples by subsequent optical measurement of the bond zone through its fracture surface. This transition is shown by the linear trend of the breaking load up to 11 kJ discharge energy and the parabolic curve shape above 11 kJ. The reason for this change is a transition in the bond zone microstructure and is discussed in Chapter 5:.

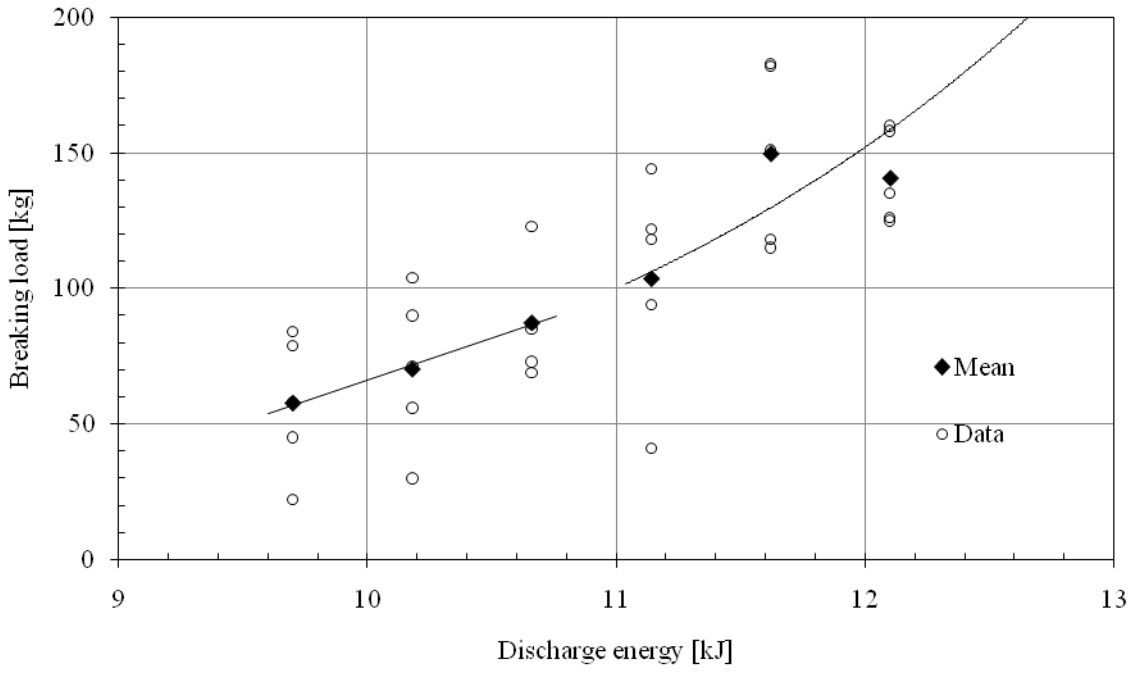


Figure 4.13: Plot of joint breaking load (kg) vs. capacitor discharge energy (kJ) for 36 Mg-Mg MPW welds.

### 4.4.3. Interface Hardness

The as-received metal hardness ranged from 80 to 95 VHN. After hardness measurements of the entire bond zone as described in 3.5.3 above, linear regression was used to create the plot of Figure 4.14. The contour plot makes it easier to visualize the overall hardness of the bonded interface. Overall hardness increase over the base metal is significant being approximately 50% harder near the start of the bond zone. Hardness decreases gradually from ~135 to ~115 VHN along the welding direction at the interface. Base metal hardness is found again at a distance of ~150 μm away from the interface.

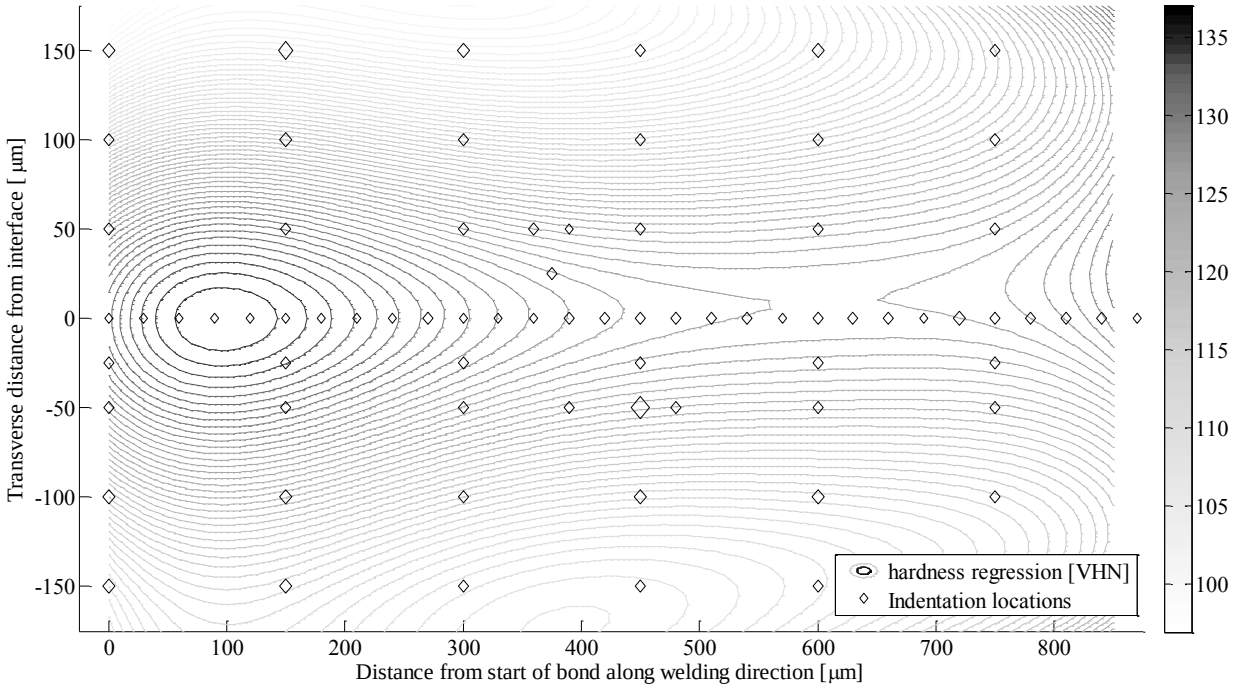


Figure 4.14: Regression contour plot showing the entire interface bond zone Vickers hardness with the indent locations from Figure 3.10.

## 4.5. Joint Microstructure

This section presents the results of metallurgical analysis of the weld's cross section microstructure in the bond zones and the unbonded centre zone. Optical microscope, SEM, TEM, and XRD, were used to observe the cross section of welds having both a straight and a wavy interface.

### 4.5.1. X-ray diffraction results

Figure 4.15 shows the x-ray diffraction peaks that were taken from four different locations in the MPW joint cross section. The locations are shown on the right side in the bottom-up order: as received sheet, unbonded centre zone sheet mid-thickness, bond zone, and bond zone sheet mid-thickness. The circle indicating location is also representative of the size (∅300 µm) of the beam irradiated area relative to the joint. The figure also shows lines whose slope represents the peak height ration between key slip planes. It is not possible to compare the intensities of the peaks from the four different areas because of the use of arbitrary units in their measure. Thus, the useful data are the ratios. These ratios indicate changes in texture.

The only significant increase in the ratio of the number of pyramidal planes reflecting to that of prismatic planes is in the bond zone, at 2.8. The other notable result is the highly increased ratio of second order pyramidal twin planes versus that of basal plane reflection which occurs throughout the entire joint thickness adjacent to the bond zone.

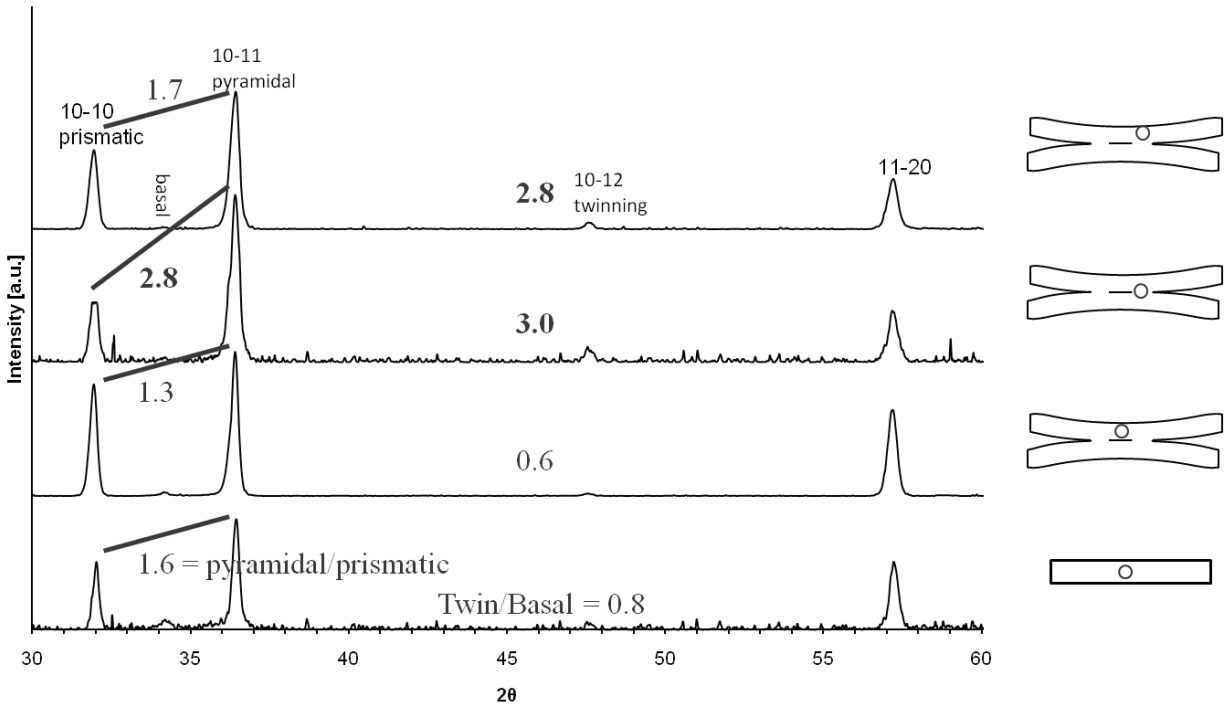


Figure 4.15: XRD diffraction peaks gathered from four different locations of the joint and relative peak heights.

### 4.5.2. Unbonded Centre Zone

Figure 4.16a shows the entire low magnification image of the unbonded centre zone. There is a fairly wide gap from impact rebounding of the sheets. In this zone are found 45° (±20°) crossing bands throughout the full thickness of the sheets; observed in Figure 4.16a. As illustrated in Figure 4.16b, the majority of plastic deformation and twinning was confined within these shear bands while the adjacent grains were largely not deformed. The surface cracks shown previously in Figure 4.8a originate and propagate along these shear bands.

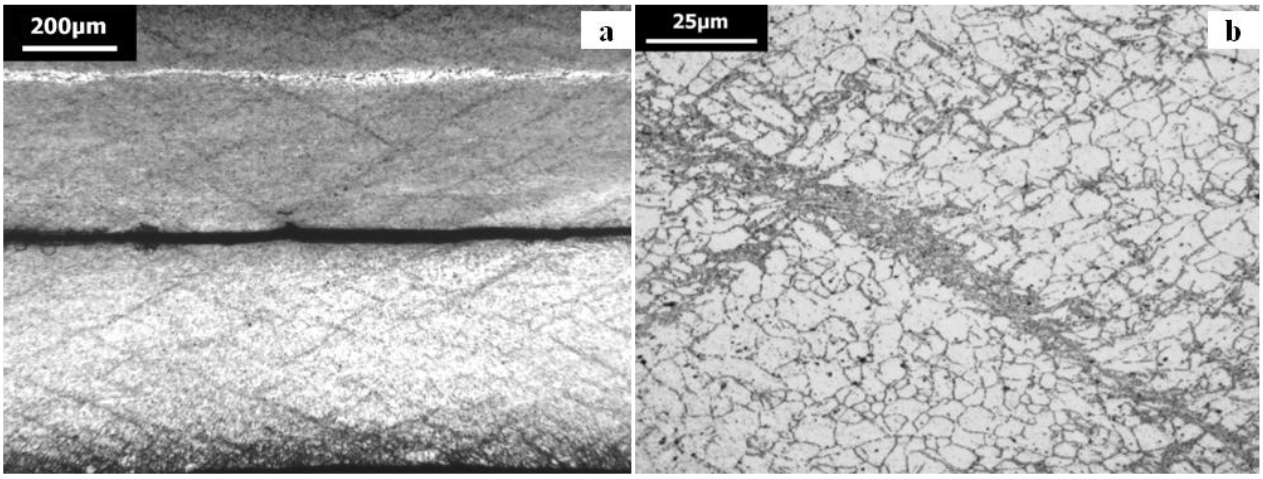


Figure 4.16: Photomicrographs showing (a) the unbonded centre zone in low magnification and (b) the close-up of a shear band.

A peculiar feature found in the cross section is shown in Figure 4.17, and is also visible in Figure 4.16a. A 10 - 20 µm thick band of light etching material, typically spanning the length of the unbonded centre zone, was observed at mid-thickness of the sheet. Typically this band was found only on one of the sheets though it also sometimes appeared on both and could be as long as the entire impacted area. The microhardness of this band was not significantly different from adjacent material.

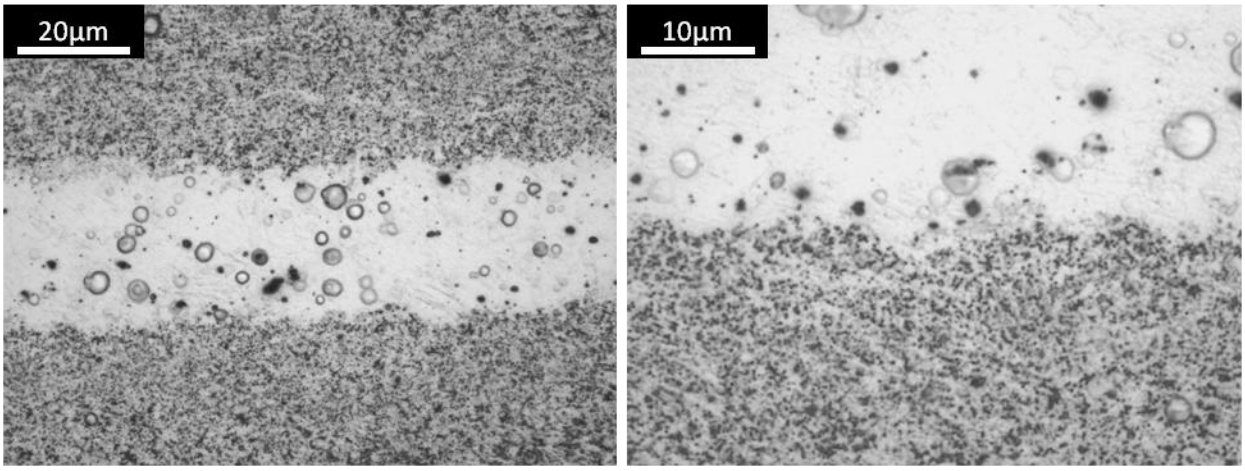


Figure 4.17: Light etching band in mid-thickness of sheet along the impacted surface.

### 4.5.3. Bond Zone

#### *4.5.3.1. Welds made with Al interlayer*

First cross section images presented are those of the welds made with an aluminum interlayer as described in 3.2. Figure 4.18a and b show the bond zone and interlayer clearly. A change from straight to wavy interface throughout the bond is evident. The soft aluminum made for a very wavy interface. In some areas the waves are on both sides of the interlayer and in other areas only on one Mg sheet. Figure 4.18c contains the EDS analysis results of the Al interlayer and shows that trapped within it are contaminant and oxide particles. Figure 4.18d shows a high magnification close up of the contact between the Al and Mg, a high level of grain refinement is visible on the etched Mg side. No resolidification or evidence of fusion is found. No intermetallic phases are found. No further investigation of the Al interlayer welds was made.

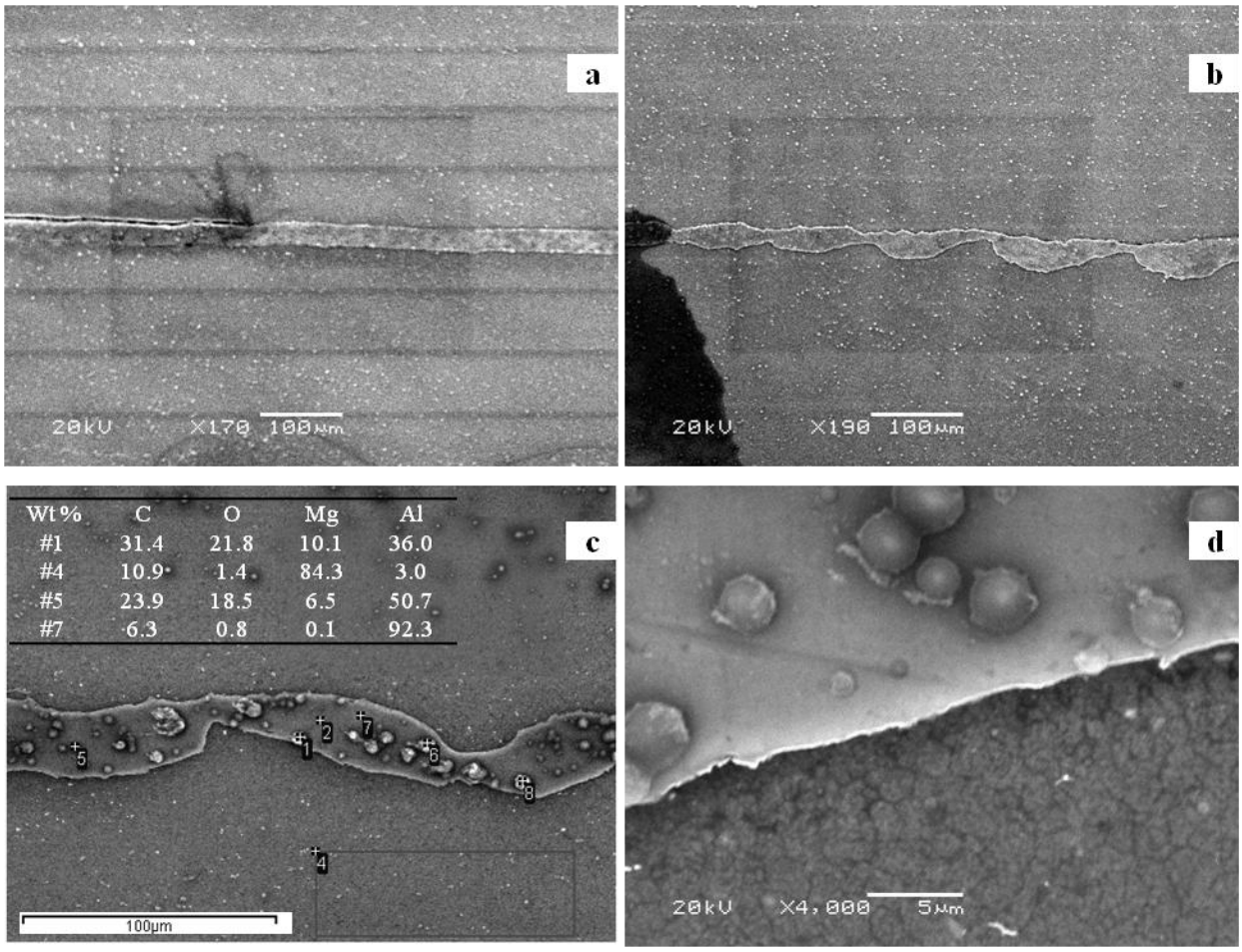


Figure 4.18: SEM images from the cross section of a weld made with Al interlayer. (a) The beginning of bond zone having straight interface and (b) wavy latter part of the same bond zone. (c) EDS analysis results of the Al interlayer. (d) High magnification of the interlayer to magnesium interface (Mg darker).

#### *4.5.3.2. Direct Mg to Mg welds*

Figure 4.19 contains optical and SEM micrographs showing the weld interface within the bond zone of the Mg to Mg magnetic pulse weld. Unlike in the unbonded centre zone, the diagonal shear bands were not observed in the bond zone. Heavy twinning can be seen uniformly throughout most of the sheet thickness as shown in Figure 4.19a. The deformation of the bulk of the sheet occurred uniformly with no strain localization within shear bands adjacent to the bond zone.

The weld cross sections of Figure 4.19 show the relatively flat or straight interface (marked by arrows). This is the interface of samples made at lower discharge energy (below 11 kJ in Figure 4.13). The entire interface of these samples was straight with no interfacial waves. Grains are difficult to distinguish at the interface in Figure 4.19a due to having been refined to a very small size. Large amount of cold work also affected the etching in this area. Within approximately 20-40 μm on each side of the interface, there is a concentration of deformation, seen from the high magnification of the SEM image of Figure 4.19b. Heavy plastic flow and elongation of the grains is visible near the interface. Grains are elongated in the welding direction symmetrically on either side, indicated a material flow at the interface. No secondary phases or resolidification is found, nor any porosity or other large defects. This is clearly a solid-state bond.

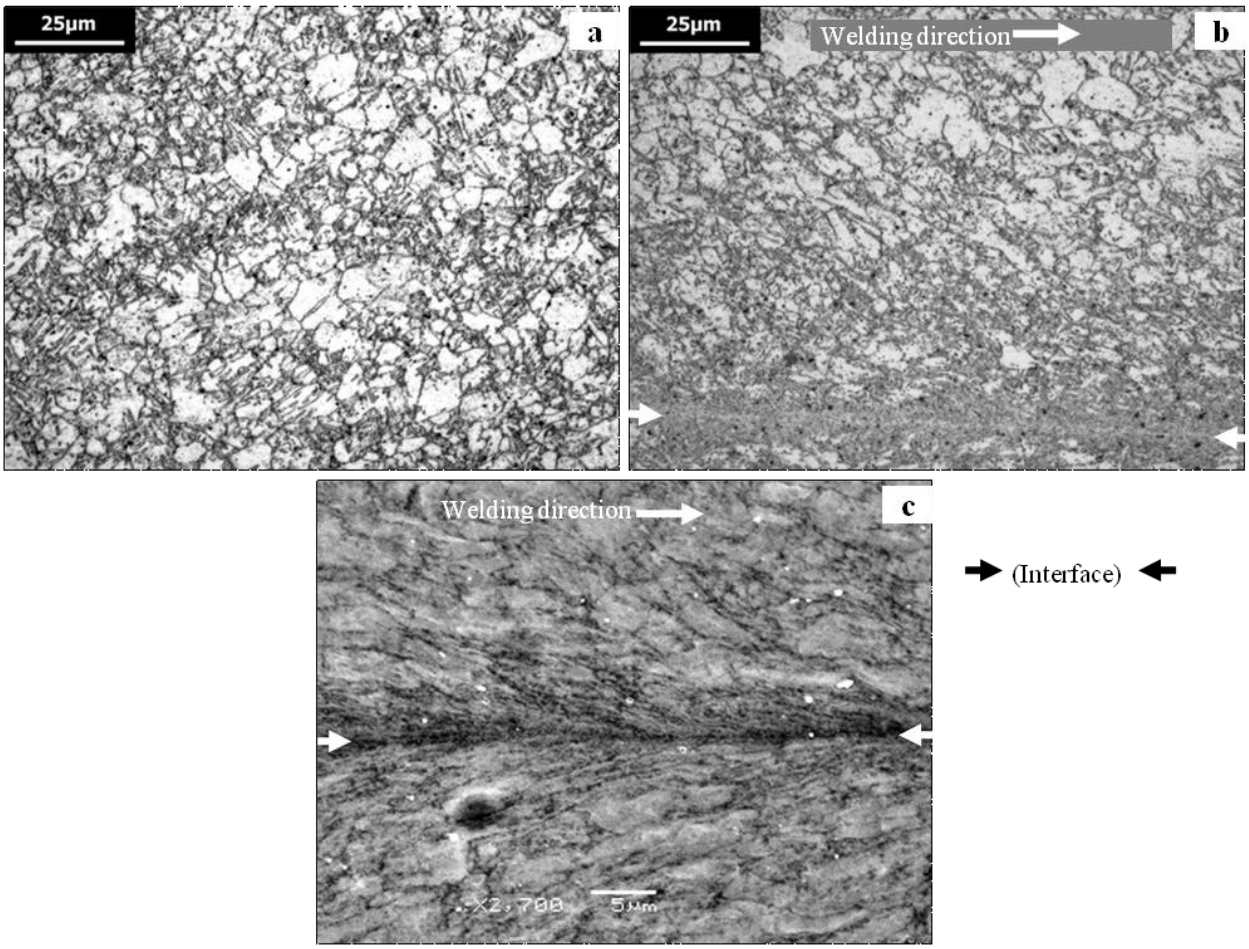


Figure 4.19: (a) Uniform heavily twinned microstructure adjacent to the bond zone. (b) Optical and (c) scanning electron microscope images of the bond zone. Weld made using 9.7 kJ discharge energy.

#### *4.5.3.3. TEM of straight interface*

TEM observation of the straight interface welds was done with the JEOL JEM-3010 machine as described in 3.5.6. Due to its small size, it was difficult to thin an area for TEM viewing directly on the interface using ion beam milling. The images of Figure 4.20 show the microstructure nearby the interface. In Figure 4.20a a stitched image is presented of an ion beam milled hole. The thinned material near the hole shows very fine grains that have a low dislocation density. This hole is nearby the interface. However, the material at the precise location of the interface line was too thick to observe. Another feature of the microstructure is seen in Figure 4.20b. It is a small section with a nano-sized lamellar structure. This lamellar pattern was observed intermittently in the area in small patches. It is not twinning as can be seen from its inset diffraction pattern. Figure 4.20c shows a typical highly refined grain, which are found nearby, approximately 1 μm in diameter.

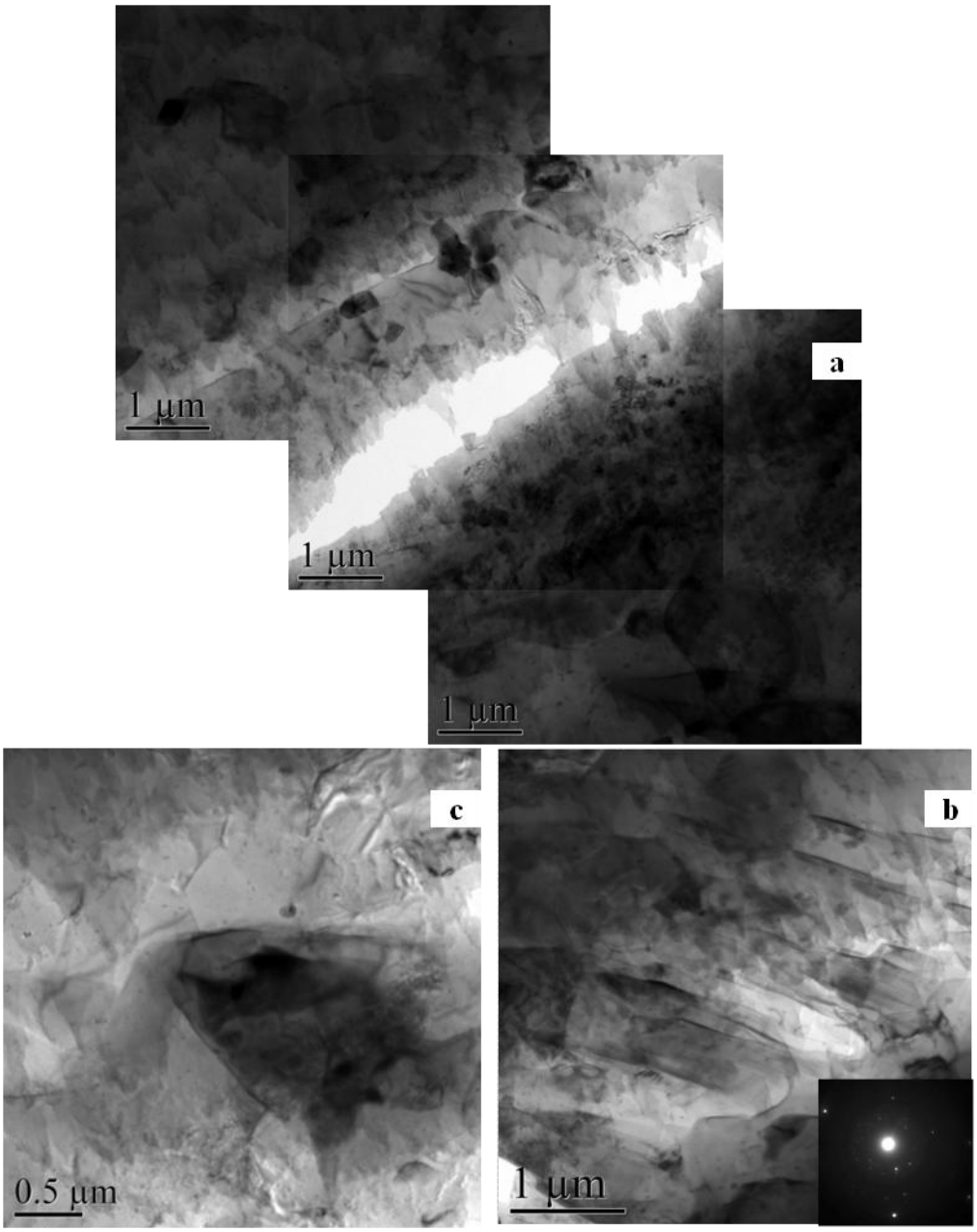


Figure 4.20: Ion milled TEM sample images from material nearby the straight interface bond zone of low discharge energy welds. (a) Stitched image of ion beam thinned hole, (b) nanoscale lamellar structure, and (c) a typical mechanically refined grain approx. 1 μm in diameter.

#### *4.5.3.4. TEM of wavy interface*

TEM of the welds with a wavy interface, that is, those welded using higher energy, was done with a TEM sample made using FIB. The FIB technique makes it easy to precisely locate and prepare only the area of interest for TEM observation. This is useful for viewing the wavy interface which formed in the higher energy welds. In these welds the latter part of the bond

zone contained interfacial waves and a thin interlayer, as seen in Figure 4.21. The SEM image of Figure 4.21b shows the interlayer and the sample as cut from it. This layer is approximately 10 μm thick at the location of the FIB cut. Although difficult to distinguish in an optical micrograph, the interlayer is clearly visible in SEM. It has a sharp contrast boundary with adjacent material, as can be seen from Figure 4.21c.

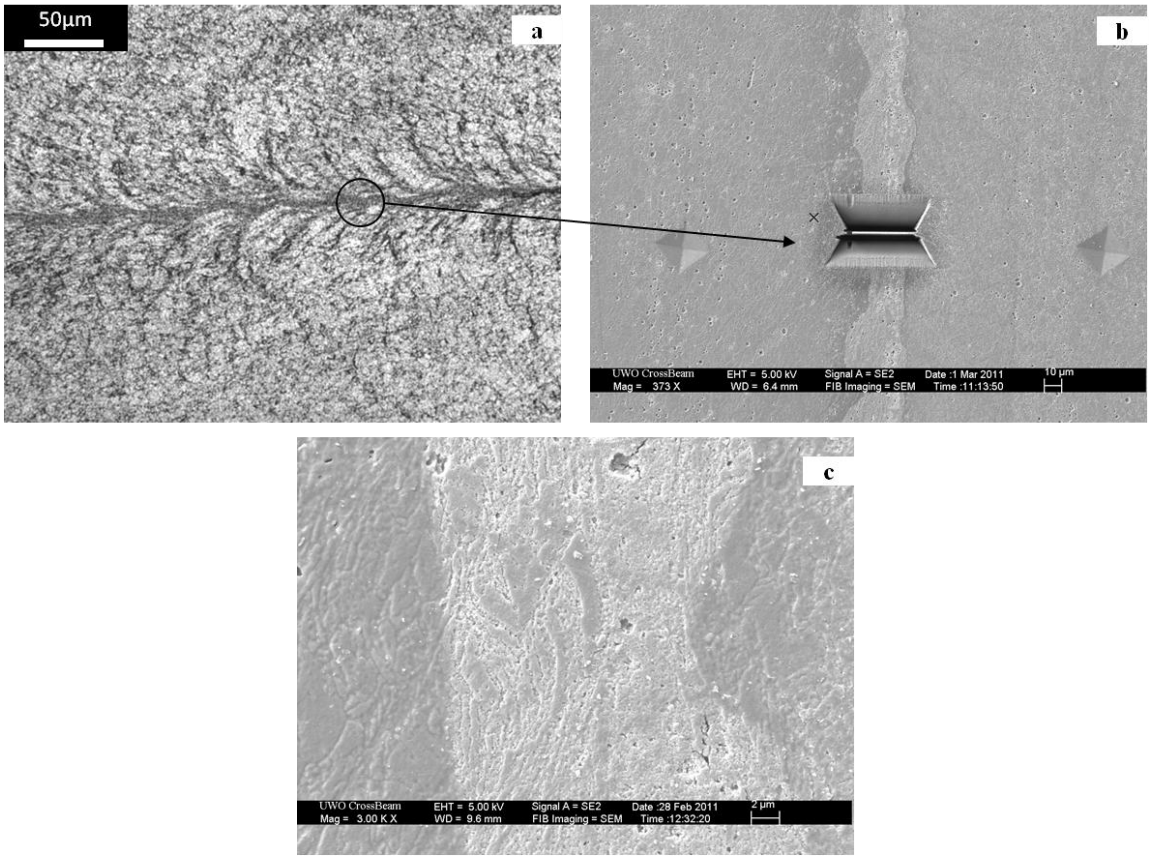


Figure 4.21: (a) Optical microscope image showing location for TEM sample, (b) The SEM image of FIB cutting location before sample removal, and (c) SEM close-up of the wavy interlayer. Weld made using 12.1 kJ discharge.

In Figure 4.22 the stitched TEM image taken of the FIB sample of the weld interface is shown. The TEM image provides the perpendicular view of the weld interface with the welding direction being into the page. There are two regions found in the sample from the interface centre outwards: the lighter colour interlayer and a gradient transition to ultrafine grains. There is a clear, sharp and straight boundary line separating the interlayer and adjacent material. The interlayer width varied between 8 and 25 μm and the ultra fine grains were found approximately 5 – 10 μm from the boundary. At the higher magnification of Figure 4.23, the

images show interlayer boundary is sharp and clearly indicating a critical, rather than smooth, transition.

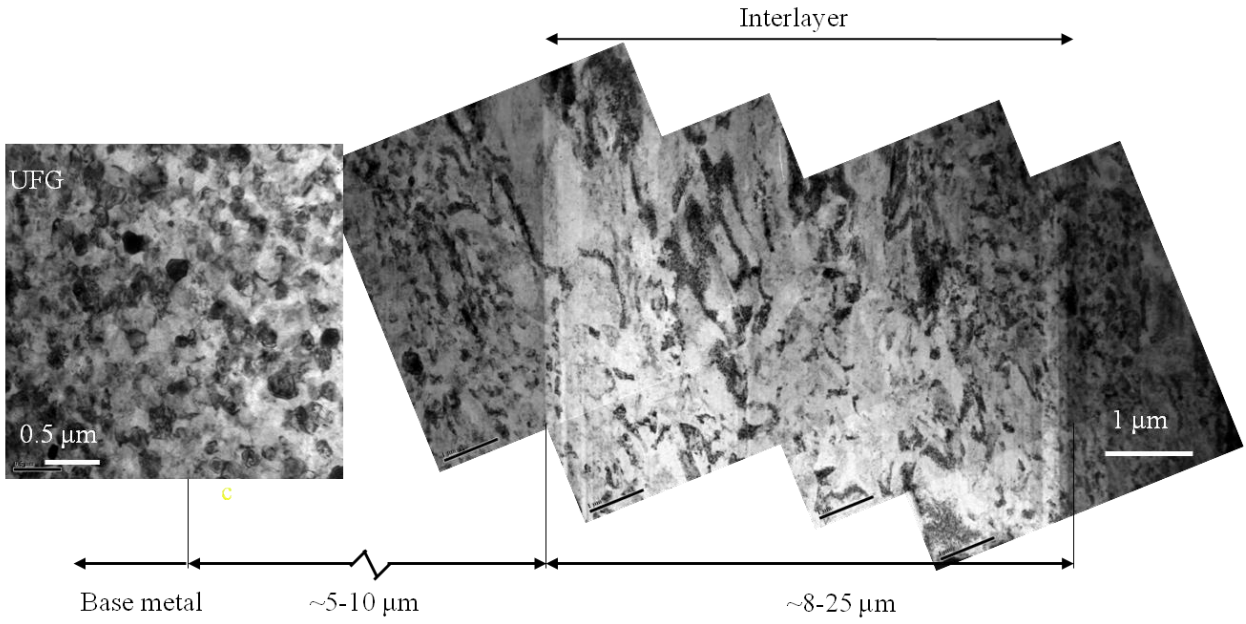


Figure 4.22: Stitched TEM image of the weld interface including the interlayer.

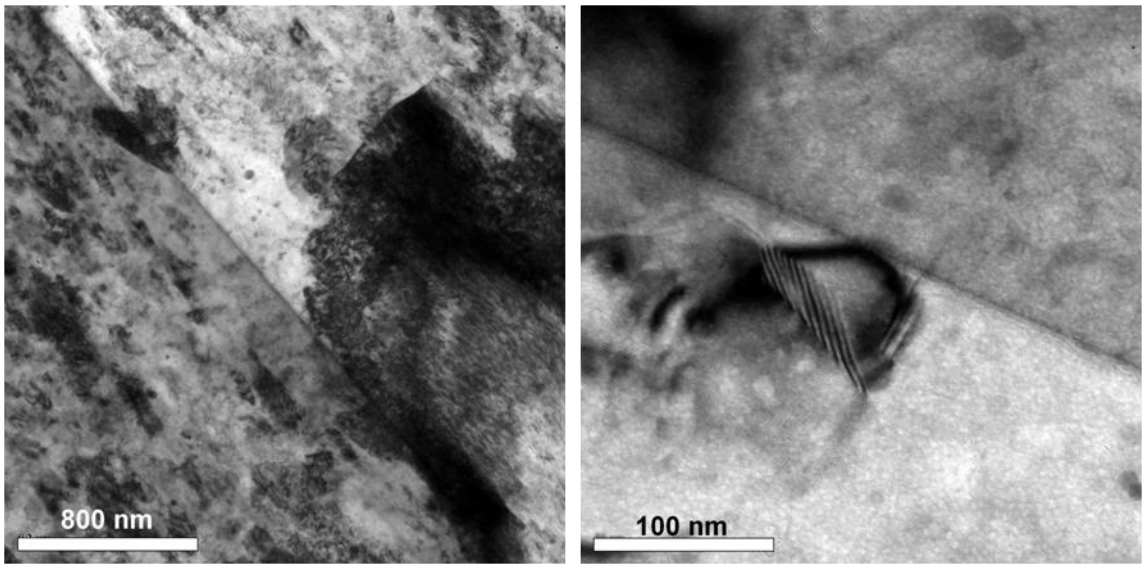


Figure 4.23: High magnification TEM images of the sharp interlayer boundary.

Figure 4.24a shows the TEM image of the interlayer at a higher magnification. It is found that within the interlayer grain boundaries are difficult to distinguish and the main structural feature is that of dispersed dislocation cells that are seemingly flattened. The grain size in the

interlayer is relatively large even though this is the area of highest strain. The appearance of the interlayer grains is not of mechanical refinement. However, some directionality is evident as indicated by the Selected Area Electron Diffraction (SAED) pattern of the interlayer.

From Figure 4.24b: the adjacent material next to the interlayer has similar features as the interlayer having the dislocation cells and flattening. The structure of this region forms a gradient transition between the interlayer and the ultrafine equiaxed grains of Figure 4.24c that were observed approximately ~5 μm away from the interlayer centre. The ultrafine grains are less than 300 nm in diameter and have no particular texture as indicated by a polycrystalline-like SAED pattern. Further away from the interlayer, elongated "base metal" grains in the welding direction were eventually observed (see Figure 4.19).

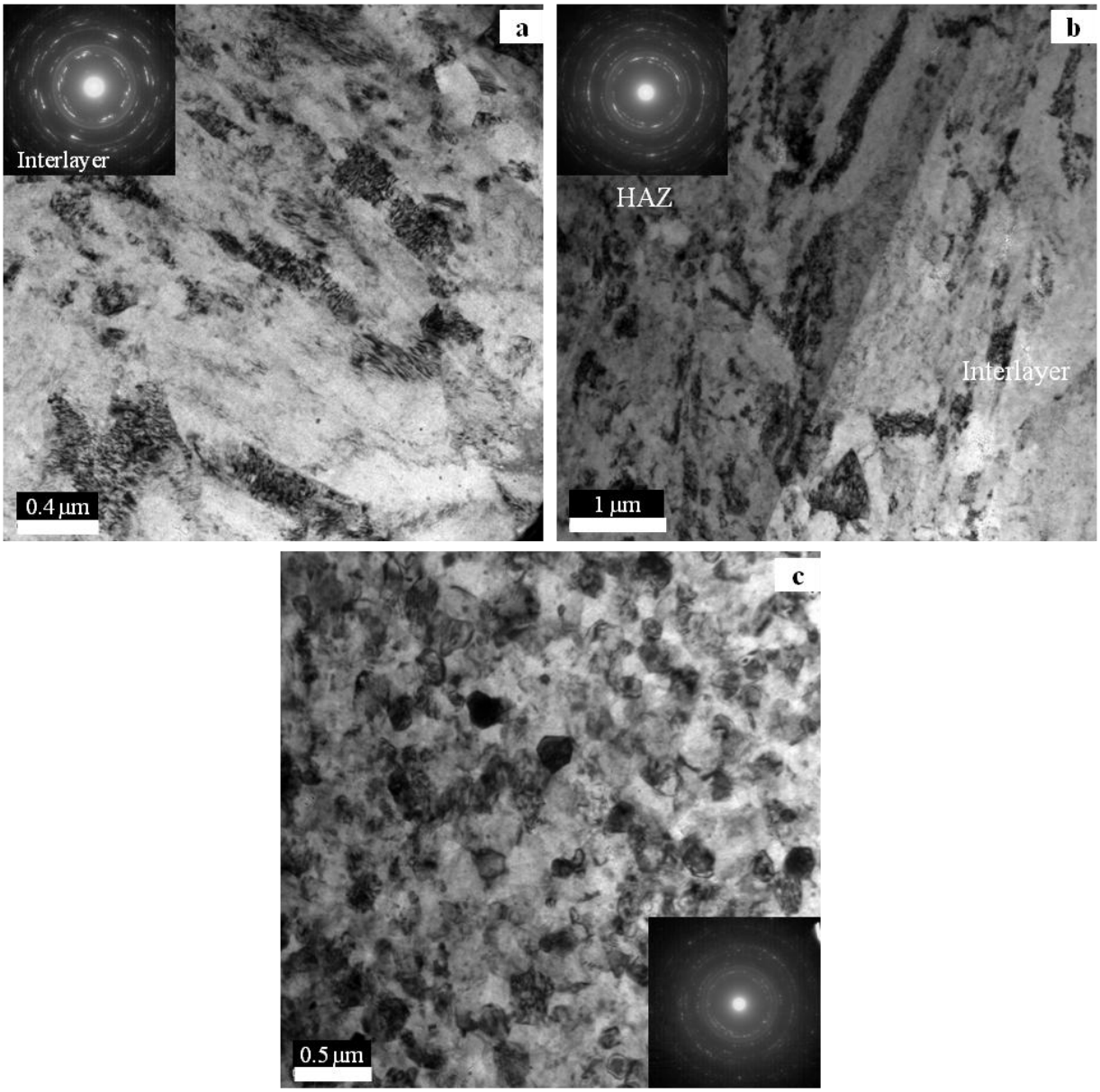


Figure 4.24: TEM images and respective selected area electron diffraction (SAED) patterns: (a) interlayer, (b) adjacent material to the interlayer (HAZ) showing boundary with interlayer, and (c) ultrafine equiaxed grains observed nearby the interlayer.

A few locations along the interlayer boundary were found where the boundary disappeared or was somewhat broken up and ultrafine grains appeared in that area. Figure 4.25 shows two of such areas. The ultrafine grains are indicated by the dashed ovals and arrows marked the boundary. The contrast difference between the interlayer and the other material in these areas is lower.

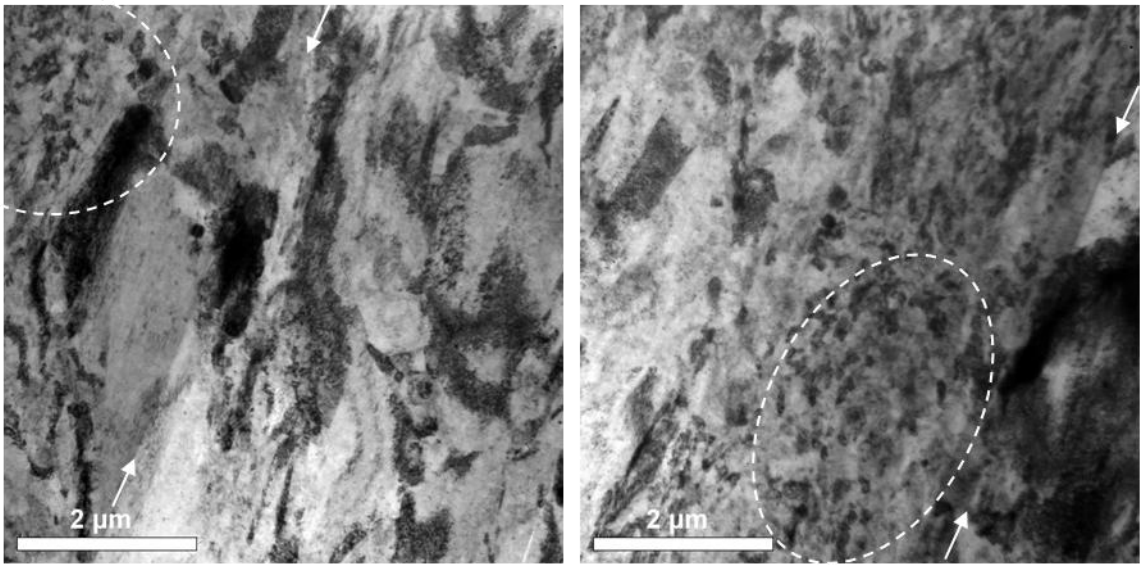


Figure 4.25: TEM images showing a short break in the sharp interlayer boundary with appearance of patches of ultrafine grains.

#### *4.5.3.5. Resolidified interface*

Several special welds were made using high discharge energy to induce melting at the interface. Figure 4.26a shows a turbulent wavy interface with a thick interlayer of resolidified material. In (b) of the same figure is a high magnification detail of the porosity inside it. Figure 4.26c is a further close-up of one of the vortices on the wave. The amplitude and wavelength of these interfacial waves is relatively small, not larger than those seen in the Al interlayer welds (section 4.5.3.1) attesting to the low ductility of this material. The grains immediately adjacent to the melted interface have a very small size.

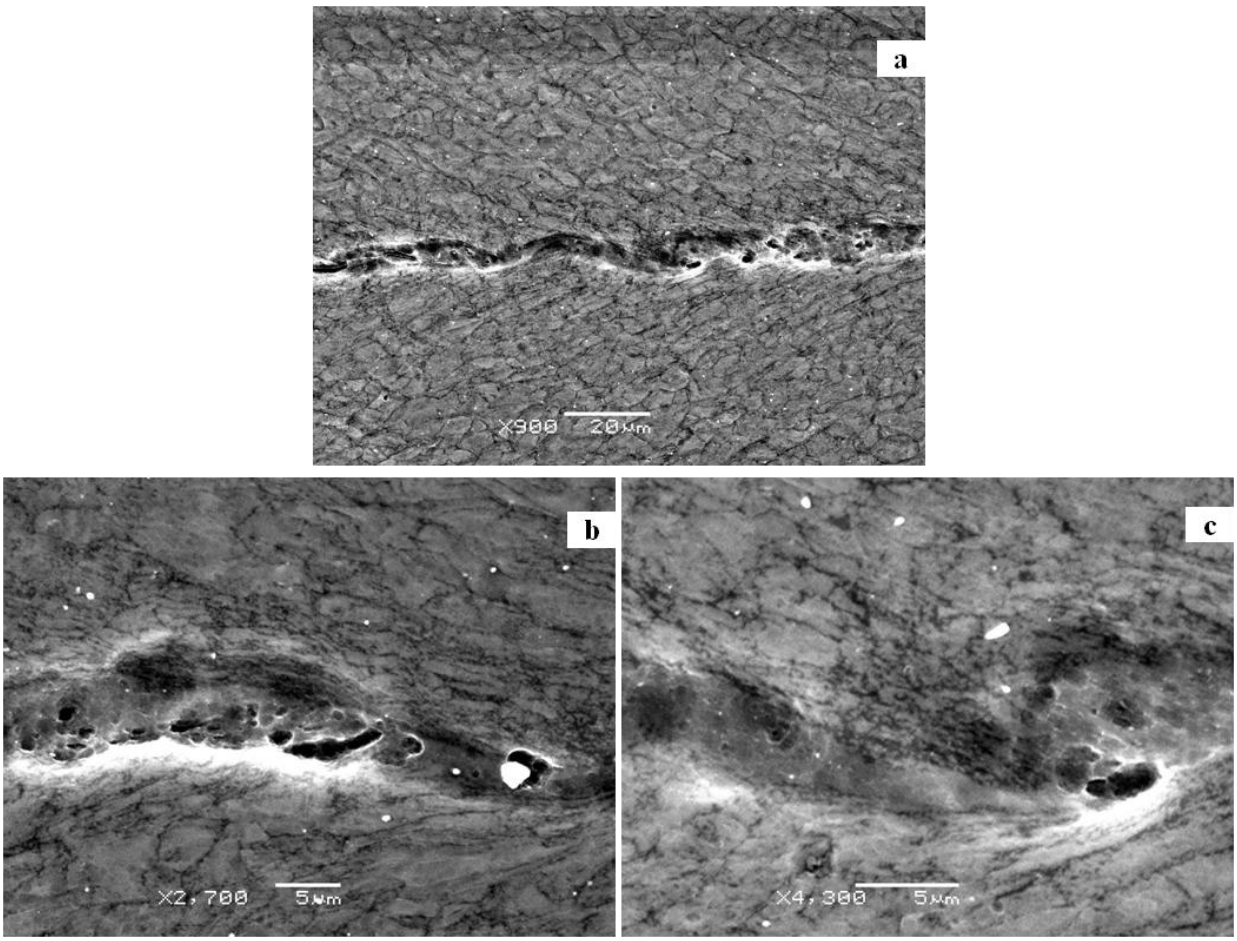


Figure 4.26: Evidence of melting at the weld interface of some welds made using high discharge energy.

## Chapter 5: Discussion

This chapter presents the relationships between the observed results of the previous chapter. It attempts to extract a generalization regarding the mechanical performance of the MPW joint as related to the interface microstructure as well as with the other objectives of the study. Agreement with previous work is assessed, and explanations for exceptions in the data are provided. Also mentioned are the limitations and weaknesses of the experimental approach of this study. Lastly, the theoretical implications and practical application aspect are discussed.

From among the objectives of this study is the need to understand the joint morphology of these lap welds made with MPW and establish an early connection of the microstructure with the mechanical properties. As well as to set a developmental point from which further probing can be made in terms of bond metallurgical aspects. In improving the understanding of the effect of microstructure on strength, an approach can be made to improve the practicality.

The unique and reluctant behaviour of Mg in deformation can undermine its feasibility of joining using most solid-state welding techniques, let alone with violent Impact Welding. The lack of attempts to joint Mg in explosion welding, the most common impact welding method having extensive research background, shows the hesitation of the community with regard to welding it this way. Thus the establishment of the feasibility of MPW for this material was a point of originality for this work.

With the given, available time and resources, the type of investigation undertaken was primarily a metallurgical characterization touching only the surface of mechanical testing. After a brief optimization period in equipment, sample, and welding conditions (see Chapter 3:) a number of welds were produced for tensile-shear testing and a number for cross-sectioning. Data collection was mainly through various analytical metallurgy techniques. Observation of the cross section in bonded and unbonded areas of the interface was done using these methods to form the bulk of the results in Chapter 4:. This chapter discusses the relevance of the results in light of the objectives and also explains results that provided limited insight.

## 5.1. Joint Morphology

The interesting joint morphology that occurs with flat sheet lap MPW welds made with any material, that is, having twin bond zones situated about an unbonded centre, can be explained by the changing of the collision angle (β) throughout the welding process. Figure 5.1 illustrates β and schematically represents the deformation taking place during double sided MPW, as carried out in this study. The dissection of the stages of the flight and welding are as follows. Due to the repulsive interaction between the two opposing magnetic fields, driving pressure was formed on one side of each Mg sheet. This caused a uniform free bulging deformation in each sheet. The initial contact between the sheets was normal and the angle β was negligibly small. Given the symmetry of the contact, each bulge acted as a rigid barrier to the other's forward motion. However, due to the driving pressure behind each sheet, the bulges flattened against one another. As a result, two collision fronts progressed symmetrically outwards from the initial contact area of the bulge peaks. Each one of the twin bonds had the exact opposite welding direction of the other. In addition, β at each front increased continuously and its value passed through the suitable range for bonding. Within this range, jetting occurred, forming the bond. Outside of the collision angle's suitable range, surface contaminants and oxides were not removed as can be seen in the unbonded centre zone in the SEM image of Figure 4.7.

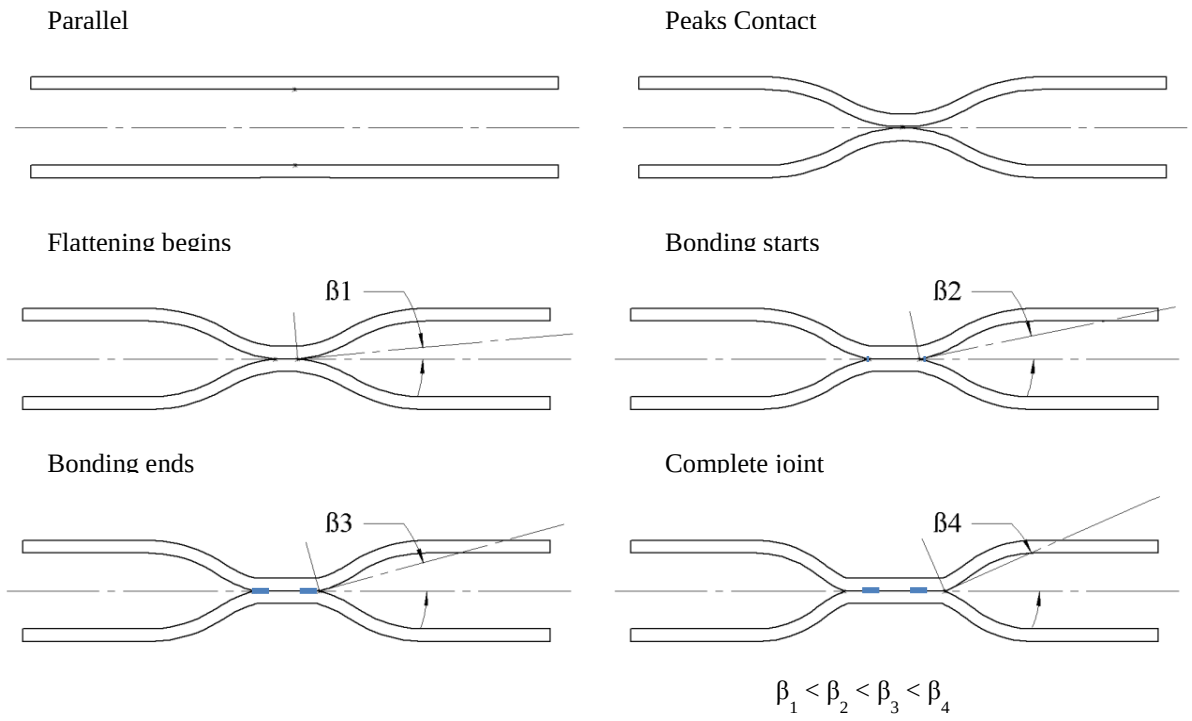


Figure 5.1: Schematic diagram showing the initial impact and flattening of the sheets during MPW.

This morphology of the joint, i.e., from the unbonded centre zone to the bond zone and then to the unbonded outer zone, is similar to the observations of Watanabe *et al.* [40]. However, in their work, Al to Al Magnetic Pulse welds were not symmetric because of the single sided experimental setup in which only one sheet was driven into the other stationary sheet. Using high-speed video, Watanabe observed that the bulged region length remained constant throughout the process and thus β continuously increased. This means that the driving pressure was not expanding in volume but only magnitude. In a single sided configuration the caveat is that some energy is absorbed by the die as it bends from the impact, this can have an effect on the transient nature of β.

## 5.2. Unbonded Centre Zone

The microstructure observed in the unbonded centre zone strengthens the above explanation of the morphology and the lack of bonding. The appearance of the diagonal shear bands seen in Figure 4.16 indicates a low β angle in this region. This is because during the twin roll casting manufacturing process, the alloy sheet is produced with such a texture that the normal axis to the close-packed planes or c-axis of the hexagonal close-packed crystal structure in most grains

is oriented perpendicular to the rolling direction. During MPW, the material within this zone experienced a compressive loading along the c-axis. This loading direction is unfavourable to basal slip. Since the basal slip system has a many times smaller CRSS than the other systems most of slip occurs along the basal planes of HCP. This normal compressive loading caused localized shear strain to develop through twinning along the $\{10\bar{1}2\}$ family of planes [59]. This twinning and double twinning within it caused a rotation of the grains into a more favourable basal slip orientation [53,59] in small localities. This formed the 45° (±20°) bands observed in Figure 4.16. The twinning was confined within these shear bands while the adjacent grains remained relatively undeformed. If the loading in this region was not perpendicular or close to perpendicular to the sheet surface, basal slip and other systems would have been activated and deformation would not be localized in bands (which was observed adjacent to the bond zone). Therefore, unlike aluminum or other materials welded with MPW, this microstructural feature of shear banding in Mg serves to confirm the normal nature of the initial impact and relates it to the lack of bonding.

In the bottom two curves of Figure 4.15, the XRD results show the diffraction peaks from the as-received and unbonded centre zone cross sections. The difference in the peak height ratios between the two is not significant. This is expected since the high degree of strain localization in the shear bands left most of the irradiated material unperturbed and thus no major texture changes occurred.

The unbonded centre zone makes no contribution to the mechanical strength of the joint and therefore its size should be minimized. From Figure 4.6 it appears as though the length of this zone coincides with the width of the current concentrator so it can be assumed that reducing the width can reduce the unbonded length. Kore *et al*. [38] showed that a tapered, or wedge like, concentrator cross section may increase the length of the bond zone. However, he did not comment on its effect on the unbonded centre zone length. The wedge concentrator shape was suggested and discussed in Figure 4.4 of 4.2.1 and further recommendations can be found in 6.2. There is a limit to how thin the concentrator can be since it then only becomes weaker and deteriorates faster (see 4.2.1). Additional detrimental features of the unbonded centre zone are the incipient cracks forming on both sides, the impact surface cracks if deep enough, and

the shear bands which could fail first if the whole joint is placed in bending along the symmetry axis.

### 5.3. Bond Zone

Outside the unbonded centre zone, on either side, are the mirror bond zones. As seen from Figure 4.19b, shear bands did not appear throughout the sheet thickness in the bond zone. The increase in the loading angle on the sheet (collision angle) activated deformation mechanisms other than only twinning and more uniform strain occurred. The bonds are about 1 mm long each. This length is the size of bond zone along the welding direction and is controlled by the suitable range of the collision angle β in which the ejection of surface contaminate or oxide is possible. As this angle increases continuously throughout the unbonded centre zone, at the start of the bond zone it has reached the lower limit of its weldability range and thus welding initiated. The transition is sharp, indicating that jetting has a critical point. This transition is clearly evident by the sudden disappearance of the oxide layer in Figure 4.7. Similarly, the bond zone ends when β becomes too large for jetting, and again a sharp transition is visible. From the EXW literature it is clear that many factors influence the β weldability range. Some being: the geometry of the coil and its current concentrator dimension (pressure source), the initial standoff distance between sheets, the initial gap between the sheet and the coil, the sheet thickness and the mechanical and electrical properties of the material, etc.

The size of the bond zone did not change in the welding direction. However, its length grew in the transverse direction, as shown in Figure 4.9. The discharge energy of the MPW process apparently influenced the overall length of the bonded area. The lengthening is explained by considering the concentrator. During welding, the short length of the current concentrator (7 mm, see 3.3.3) created a spot-like magnetic field with the highest intensity located at the centre of the spot. As the discharge energy increased, the intensity of this field increased outwards from the centre thus bringing more and more material into the minimum energy required for bonding. As a result, the bonded area is longer in the transverse direction at higher discharge energy. Mere size of bond zone alone would not cause the increase in strength that was also observed in the longer bond in Figure 4.9. A change in the microstructure is responsible for increased strength.

The short “Sample #8” of Figure 4.9 and the other samples from Figure 4.12 that were produced using less than 11 kJ had an entirely straight interface in cross section, like the interfaces in Figure 4.19b&c. On the other hand, for welds made with more than 11 kJ, the bond interface was initially flat, but gradually developed into a wavy interface, as can be seen in Figure 4.21a. The difference between Samples #8 and #22 is then the presence of interfacial waves and it caused increased bond strength. Moreover, since the straight interface occurs only when the collision conditions are at or near the lower limit of jetting and welding [43], the preferred MPW interface would contain a larger portion of wavy than straight interface.

## 5.4. Wavy Interlayer

Waves alone may not be entirely responsible for increased strength. And the 8-25 μm thick undulating interlayer found in the wavy part of the bond zone of samples that had waves may be also be contributing (see Figure 4.21, Figure 4.22). One reason for this is that while comparing the bond zone with the fracture surface, the location of the wavy interlayer along the welding direction corresponded to the ductile micro-voids region of Figure 4.10c. This fine featured ductile fracture surface could be evidence of increased strength.

The interlayer and waves in the MPW welds were found in the latter part of the bond where β is largest. In EXW, both β and driving pressure are critical factors in jetting and in interfacial wave formation [43]. These factors influence the dissipation of energy at the interface and therefore how much wave-forming instability occurs and the amount of heat generated.

Due to the small number of TEM studies in MPW and EXW, particularly for similar material welds, and none exist for Mg; very limited information is available on the character of the interlayer in literature. The available findings [60] suggest that a sub-micron reaction layer forms in dissimilar EXW bonds. However, given the welding conditions and materials, the connection to the present work is limited.

The formation and microstructure of the interlayer is a surprising result due to its significant differences with interfaces seen in explosion welding or similar material MPW. Typically the interface area experiences the highest plastic strain and consists of ultrafine equiaxed grains. In this study, rather, the DRX grains were observed on the outsides of the interlayer (see Figure 4.22, Figure 4.24c). Such nano-scale grains are the direct result of severe shear strain

[61] or dynamic recrystallization (DRX) as observed in EXW and similar processes [53,55,62]. However, the interlayer has a dislocation cell structure and enlarged grains with poorly defined grain boundaries, which could be the result of excess heat input. Also, the sharp boundaries of the interlayer with adjacent material and its different colour indicate a critical point such as a phase change. The lack of a solidification structure and the sharp boundary mean the interlayer was in a high temperature plasticized flow, possibly in the 'mushy zone' of the phase diagram. As shown in Figure 5.2, this is the semi-solid state, at approximately 575-625 °C for AZ31. Figure 5.2 demonstrates the possible temperature gradient of the interface which accounts for the structural difference between the interlayer, the nearby nano-scale DRX grains (UFG), and the unaffected distant "base metal" (BM).

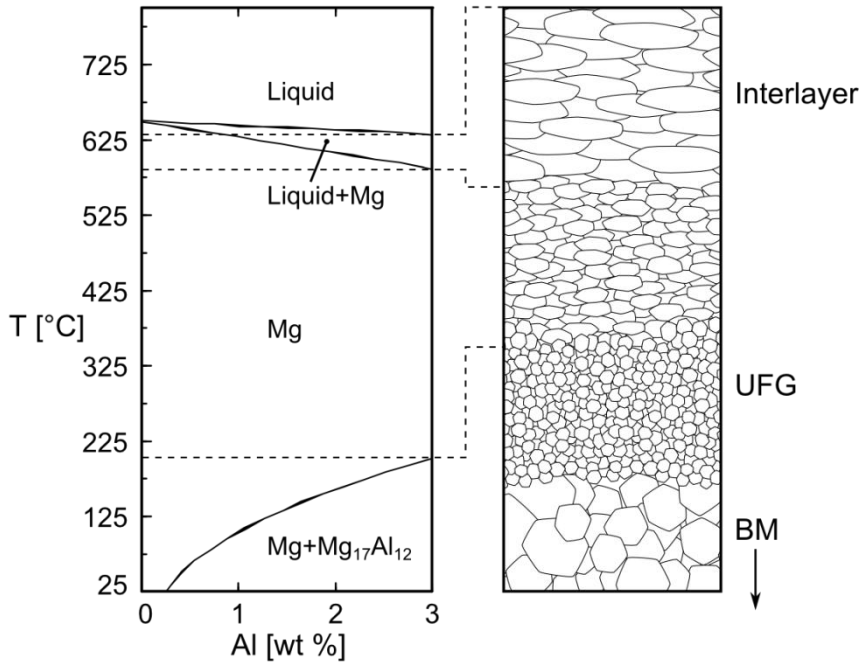


Figure 5.2: Schematic diagram of the temperatures and states in the bond zone including interlayer, ultrafine grains, and base metal grains.

With higher discharge energy, more kinetic energy would be generated in the sheets and thus more dissipation will occur at the interface, creating more heat. Higher temperatures will create a longer wavy interface and correspondingly longer interlayer. Therefore, welds made with geometry parameters (β) held constant will have an interlayer length that is proportional to the discharges energy.

## 5.5. Summary

The uniqueness of the morphology of the lap MPW welds is owed to the transient nature of the collision angle between the sheets. Using Mg for MPW showed, through microstructure, that the initial contact between the sheets is at a negligible collision angle and this is why the unbonded centre zone formed. Stronger joints resulted from increased welding discharge energy. This was found to be due to a formation of a wavy interface having a thin interlayer. The microstructure of the interlayer suggests its forming was a result of high temperature semi-solid flow, because of its contact with the cleaning re-entrant jet. This small connection between microstructure and mechanical properties can lead to further investigation of the effects of the interlayer and its exact identification. Furthermore, this can improve the understanding of welding magnesium with MPW or general impact welding and promote it as an application a step beyond its current early developmental stage.

# Chapter 6: Conclusions and Recommendations

## 6.1. Conclusions

In the present study, lap joints of AZ31 Mg alloy sheets were successfully produced using the Magnetic Pulse Welding process. The microstructure has been characterized and a link between interlayer microstructure and strength was made. Specifically, the conclusions reached include:

1) MPW produced a solid state weld between Mg sheets; no porosity or resolidification was observed and no new phases were formed at the interface.
2) The joint morphology consisted of three distinct regions observed in cross section: an unbonded centre zone ~3 mm wide, twin bond zones ~1 mm wide, and the outer unbonded surfaces which span the rest of the impact flattened area.
3) Diagonal shear bands in the unbonded centre zone confirm that bonding did not occur there due to a very low collision angle, $\beta$ in the initial contact of the sheets. $\beta$ is transient throughout the impact.
4) The bond displayed high shear strength approximately equivalent to or higher than the base metal shear strength.
5) Severe plastic deformation occurs at the interface and up to 20 μm adjacent to it with grains refined to a sub-micron diameter. ~300 μm equiaxed DRX grains exist at the interface.
6) Increase in discharge energy causes the appearance of interfacial waves. Wave amplitude increases with energy.
7) A ductile fracture surface is found to coincide with the wavy interface location; displaying very fine micro-voiding features.
8) An 8-25 μm wide layer forms at the interface corresponding with the interfacial waves.
9) The interlayer consists of a dislocation cell structure and was formed as a result of flow in a semi-solid state, at elevated temperature.
10) Welds made at higher discharge energy, containing waves and an interlayer, have a higher strength than bonds with only a straight interface.

## 6.2. Recommendations

- High variability in the mechanical properties of the welds is attributable to use of Al driver sheets on the Mg. With the use of these sheets, the uniformity of the impact becomes a question of the uniformity of contact between them and the Mg sheets, since both are not perfectly flat. A possible mitigation is to roll the Mg and Al sheets together prior to welding. Because of the softness of the Al, the thickness of the Mg would not change and the contact area between them would increase.
- The effect of incipient cracks that form on both sides of the bond zones can be investigated by partial tensile shear testing.
- Mechanical and electromagnetic coil design literature is scarce. MPW research has primarily relied on trial and error to design coils. It may be possible to investigate this further with an electromagnetic-mechanical coupled FEA.
- The MPW-20 machine does not have sufficiently high frequency to efficiently drive Mg. From skin depth calculation approximately 80 kHz is required to fully contain the magnetic field within a 0.6 mm Mg sheet.
- It is probable that a 1MHZ camera could be used to study the actual value of $\beta$ and the collision point velocity and thus provide a material specific welding window of these values for Mg.

## References


[1] Blazynski T. Z., 1983, “Explosive Welding, Forming and Compaction.”

[2] Gaines L., Cuenca R., Stodolsky F., and Wu S., 1996, “Potential Automotive Uses of Wrought Magnesium Alloys,” Automotive Technology Development, Detroit, Michigan.

[3] Smith W. F., 1993, Structure and Properties of Engineering Alloys, McGraw-Hill.

[4] Zhang P., 2003, “Joining enabled by high velocity deformation,” The Ohio State University.

[5] Shreffler R. G., and Deal W. E., 1953, “Free surface properties of explosive-driven metal plates,” Journal of Applied Physics, **24**(1), pp. 44-48.

[6] Cowan G. R., and Holtzman A. H., 1963, “Flow Configuration in Colliding Plates: Explosive Bonding,” Journal of Applied Physics, **34**(4), pp. 928-939.

[7] Carpenter S. H., and Wittman R. H., 1975, “Explosion welding,” Annual Review of Materials Science, **1975**(5), pp. 177-199.

[8] Reid S. R., and Sherif N. H. S., 1976, “Prediction of the wavelength of interface waves in symmetric explosive welding,” Journal of mechanical engineering science, **18**(2), pp. 89-94.

[9] Akbari Mousavi A. A., and Al-Hassani S. T. S., 2005, “Numerical and experimental studies of the mechanism of the wavy interface formations in explosive/impact welding,” Journal of the Mechanics and Physics of Solids, **53**(2005), pp. 2501-2528.

[10] Crossland B., 1982, Explosive Welding of Metals and its Application, Oxford Science Publications, Oxford.

[11] Kowalick F. J., and Hay R., 1971, “A Mechanism of Explosive Bonding,” Metallurgical Transactions, **2**(July), pp. 1953-1958.

[12] Bahrani A. S., Black T. J., and Crossland B., 1966, “The mechanics of wave formation in explosive welding,” Proceedings of the Royal Society of London. Series A, Mathematical and Physical Sciences, **296**(1445), pp. 123-136.

[13] Godunov S. K., Deribas A. A., Zakharenko I. D., and Mali V. I., 1971, “Investigation of the viscosity of metals in high-velocity collisions,” Fizika Goreniya I Vzryva, **1**(1971), pp. 135-141.

[14] Cowan G. R., Bergmann O. R., and Holtzman A. H., 1971, "Mechanism of bond zone wave formation in explosion-clad metals," Metallurgical Transactions, **2**, pp. 3145-3155.

[15] Abrahamson G. R., 1961, "Permanent periodic surface deformations due to travelling jet," journal of applied mechanics, **28**(4), p. 519.

[16] Robinson J. L., 1975, "The mechanics of wave formation in impact welding," Philosophical Magazine, **31**(3), pp. 587-597.

[17] Gordopolov Y. A., Dremin A. N., and Mikhailov A. N., 1978, "Theory of waves on the interface of metals welded by explosion," Fizika Goreniya I Vzryva, **14**(4), pp. 77-86.

[18] Dudin A., 1971, "Tube welding with a pulsed magnetic field," Svarochnoye Proizvodstvo, **2**, pp. 16-18.

[19] Demichev V. F., 1993, "The use of Strong-Pulsed Magnetic Fields to Weld Metals," Atomnaya Energiya, **73**(4), pp. 278-284.

[20] Kojima M., Tamaki K., Suzuki J., and Sasaki K., 1989, "Flow stress, collision velocity and collision acceleration electromagnetic welding," Welding International, **4**(9), pp. 684-690.

[21] Yu-quan S., and Jun Z., 1986, "A Mechanical Analysis of the Superplastic Free Bulging of Metal Sheet," Materials Science & Engineering, **84**, pp. 111-125.

[22] Mamalis A. G., Manolakos D. E., Kladas A. G., and Koumoutsos A. K., 2005, "Physical principles of electromagnetic forming process: a constitutive finite element model," J. Mat. Proc. Tech, **161**, pp. 294-299.

[23] Mamalis A. G., Manolakos D. E., Kladas A. G., and Koumoutsos A. K., 2006, "Electromagnetic Forming Tools and Processing Conditions: Numerical Simulation," Materials and Manufacturing Processes, **21**(4), pp. 411-423.

[24] Unger J., Stiemer M., Svendsen B., and Blum H., 2006, "Multifield modeling of electromagnetic metal forming," processes. Journal of Materials Processing Technology, **177**, pp. 270-273.

[25] Correia J. P. M., Siddiqui M. A., Ahzi S., Belouettar S., and Davies R., 2008, "A simple model to simulate electromagnetic sheet free bulging process," International Journal of Mechanical Sciences, **50**, pp. 1466-1475.

[26] Thomas J. D., and Triantafyllidis N., 2009, "On electromagnetic forming processes in finitely strained solids : Theory and examples," Journal of the Mechanics and Physics of Solids, **57**(8), pp. 1391-1416.

[27] Aizawa T., 2003, "Magnetic pressure seam welding method for aluminium sheets," Welding International, **17**(12), pp. 929-933.

[28] Aizawa T., 2004, "Methods for Electromagnetic Pressure Seam Welding of Al/Fe Sheets," Welding International, **18**(11), pp. 868-872.

[29] Lee K., Kumai S., Arai T., and Aizawa T., 2007, "Interfacial microstructure and strength of steel/aluminum alloy lap joint fabricated by magnetic pressure seam welding," Materials Science and Engineering A, **471**, pp. 95-101.

[30] Ben-Artzy A., Stern A., Frage N., and Shribman V., 2008, "Interface phenomena in aluminium– magnesium magnetic pulse welding," Science And Technology of Welding and Joining, **13**(4), pp. 402-408.

[31] Kore S. D., Date P. P., and Kulkarni S. V., 2008, "Electromagnetic Impact Welding of Aluminum to Stainless Steel Sheets," J. Mater. Process. Technol, **pp**, pp. 486-493.

[32] Kore S. D., Imbert J., Worswick M. J., and Zhou Y., 2009, "Electromagnetic Impact welding of Mg to Al sheets," Science and Technology of Welding and Joining, **14**(6), pp. 549-553.

[33] Watanabe M., Kumai S., and Aizawa T., 2006, "Interfacial microstructure of magnetic pressure seam welded Al-Fe, Al-Ni, Al-Cu lap joints," Materials Science Forum, **519-521**, pp. 1145-1150.

[34] Lee K., Kumai S., Arai T., and Aizawa T., 2007, "Interfacial Microstructure and Strength of Steel/Aluminum Alloy Lap Joint Fabricated by Magnetic Pressure Seam Welding," Materials Science & Engineering, **471**, p. 7.

[35] Volobuev I., and Legeza A., 1972, "Phase transformations in joints produced by magnetic pulse welding," Svarochnoye Proizvodstvo, **8**, pp. 8-9.

[36] Song J., Kostka A., Veehmayer M., and Raabe D., 2011, "Hierarchical microstructure of explosive joints: Example of titanium to steel cladding," Materials Science and Engineering: A, **528**(6), pp. 2641-2647.

[37] Stern A., and Aizenshtein M., 2002, "Bonding zone formation in magnetic pulse welds," Science and Technology of Welding and Joining, **7**(5), p. 4.

[38] Kore S. D., Date P. P., and Kulkarni S. V., 2007, "Effect of process parameters on electromagnetic impact welding of aluminum sheets," International Journal of Impact Engineering, **34**, pp. 1327-1341.

[39] Zhang Y., Babu S. S., Zhang P., Kenik E. A., and Daehn G. S., 2008, "Microstructure characterisation of magnetic pulse welded AA6061-T6 by electron backscattered diffraction," Science and Technology of Welding and Joining, **13**(5), pp. 467-471.

[40] Watanabe M., and Kumai S., 2009, "High-Speed Deformation and Collision Behaviour of Pure Aluminum Plates in Magnetic Pulse Welding," Materials Transactions, **50**(8), pp. 2035-2042.

[41] Zhang Y., Babu S. S., and Daehn G. S., 2010, "Interfacial ultrafine-grained structures on aluminum alloy 6061 joint and copper alloy 110 joint fabricated by magnetic pulse welding," Journal of Materials Science, **45**(17), pp. 4645-4651.

[42] Zakharenko I. D., 1990, Svarka metallov vzryvom, Navuka i Tekhnika, Minsk.

[43] Liu S., Banker J., and Prothe C., 2011, "Explosion Welding," ASM Handbook Vol. 6, D.L. Olson, T.A. Siewert, S. Liu, and G.R. Edwards, eds., ASM International, Materials Park, OH.

[44] Raynor G. V., 1959, The Physical Metallurgy of Magnesium and its Alloys, Perg-amon Press, London.

[45] Reed-hill R. E., and Robertson W. D., 1958, "Pyramidal Slip in Magnesium," Transactions of The Metallurgical Society of AIME, (April), pp. 256-259.

[46] Obara T., Yoshinga H., and Morozumi S., 1973, "{11-22}<-1-123> Slip system in magnesium," Acta Metallurgica, **21**(July), pp. 845-853.

[47] Barnett M. R., 2007, "Twinning and the ductility of magnesium alloysPart II. 'Contraction' twins," Materials Science and Engineering: A, **464**(1-2), pp. 8-16.

[48] Reed-hill R. E., and Robertson W. D., 1957, "Additional modes of deformation twinning in magnesium," Acta Metallurgica, **5**(12), pp. 717-727.

[49] Ulacia I., Dudamell N. V., Galvez F., Yi S., Perez-Prado M. T., and Hurtado I., 2010, "Mechanical behavior and microstructural evolution of a Mg AZ31 sheet at dynamic strain rates," Acta Materialia, **58**, pp. 2988-2998.

[50] Gehrmann R., Frommert M., and Gottstein G., 2005, "Texture effects on plastic deformation of magnesium," Materials Science and Engineering A, **395**(1-2), pp. 338-349.

[51] Barnett M. R., Keshavarz Z., and Ma X., 2006, "A Semianalytical Sachs Model for the Flow Stress of a Magnesium Alloy," Metallurgical and Materials Transactions A, **37**(July), pp. 2283-2293.

[52] Wonsiewicz B., and Backofen W., 1967, "Plasticity of Magnesium crystals," Transactions of The Metallurgical Society of AIME, **239**, pp. 1422-1431.

[53] Zhen L., Zou D. L., Xu C. Y., and Shao W. Z., 2010, "Microstructure evolution of adiabatic shear bands in AM60B magnesium alloy under ballistic impact," Materials Science and Engineering: A, **527**(21-22), pp. 5728-5733.

[54] Barnett M. R., 2009, "The challenge of in homogenous deformation in magnesium and its alloys," Materials Science Forum, **618-619**, pp. 227-232.

[55] Murr L. E., Trillo E. A., Pappu S., and Kennedy C., 2002, "Adiabatic shear bands and examples of their role in severe plastic deformation," Journal of Materials Science, **37**, pp. 3337 - 3360.

[56] Esquivel E., and Murr L. E., 2005, "Grain boundary contributions to deformation and solid-state flow in severe plastic deformation," Materials Science and Engineering: A, **409**(1-2), pp. 13-23.

[57] Meyers M., 2001, "Shear localization in dynamic deformation of materials: microstructural evolution and self-organization," Materials Science and Engineering A, **317**(1-2), pp. 204-225.

[58] Golovashchenko S. F., 2007, "Material Formability and Coil Design in Electromagnetic Forming," Journal of Materials Engineering and Performance, **16**(June), pp. 314-320.

[59] Koike J., 2005, "Enhanced Deformation Mechanisms by Anisotropic Plasticity in Polycrystalline Mg Alloys at Room Temperature," Metallurgical and Materials Transactions A, **36**(July), pp. 1689-1696.

[60] Chiba A., Nishida M., and Morizono Y., 2004, "Microstructure of Bonding Interface in Explosively-Welded Clads and Bonding Mechanism," Materials Science Forum, pp. 465-474.

[61] Valiev R. Z., 2004, "Nanostructuring of metals by severe plastic deformation for advanced properties," Nature Materials, **3**, pp. 511-516.

[62] Murr L. E., and Pizaña C., 2007, "Dynamic Recrystallization: The Dynamic Deformation Regime," Metallurgical and Materials Transactions A, **38**(11), pp. 2611-2628.

## Appendix A: Machine Operation

In this appendix the basic steps to operating the MPW-20 machine are described.

First switch on the breaker found in the corner of the cage on the inside.


Next open the lower door of the power supply tower and make sure the 3-phase lights, R-S-T, are on. Check that the Mode is on Manual and that Auto Drain is set to ON. Turn on the gray power bar in the centre. Position the sample inside the coils and press the green start button.

Close the tower door. Leave the cage and close its door. Safety switches on both these doors must be closed to fire.


If the green start button does not turn on it is because the emergency stop button on the console is depressed. To set the charge voltage, press the second from left button on the display under "working voltage" label twice. Then set the voltage with the two right buttons.


Push cycle start, you will see the voltage value ramping up on the display until your set point. It will then fire. After the shot depress the large emergency stop button and then release it. Go inside the cage and before removing the sample or touching the coil in anyway, use the grounding sword to check for residual charge.

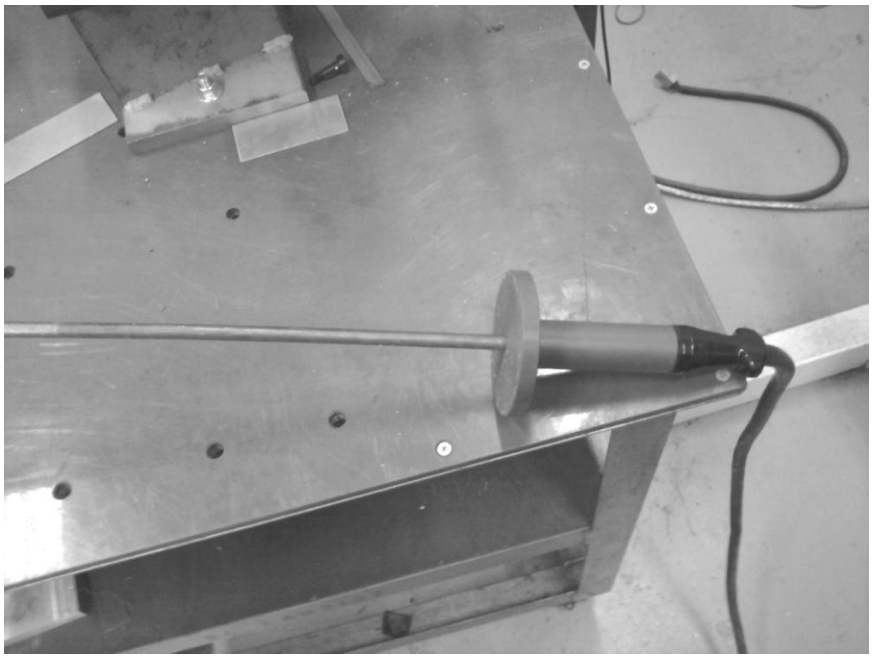

## Appendix B: Coil Drawing

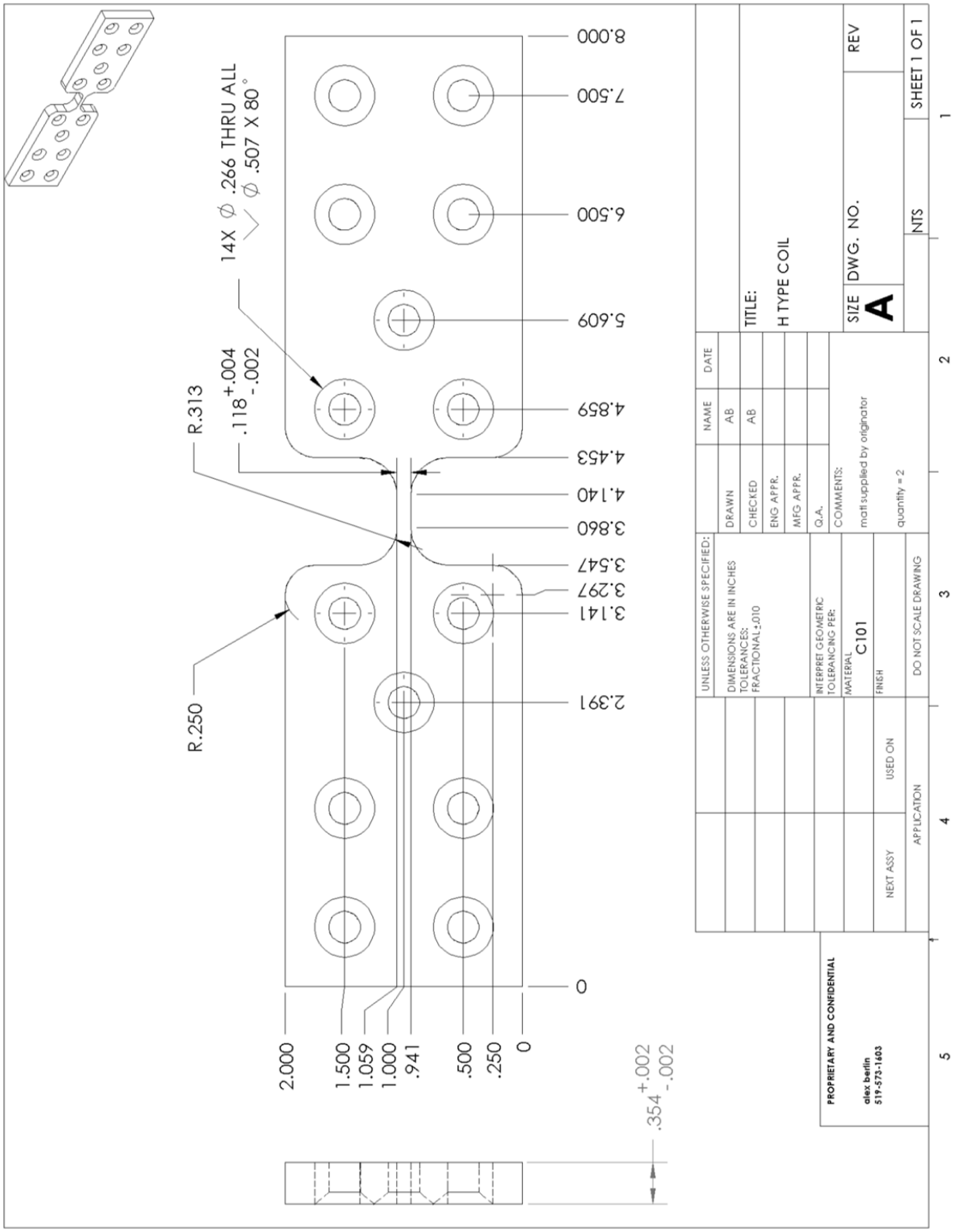

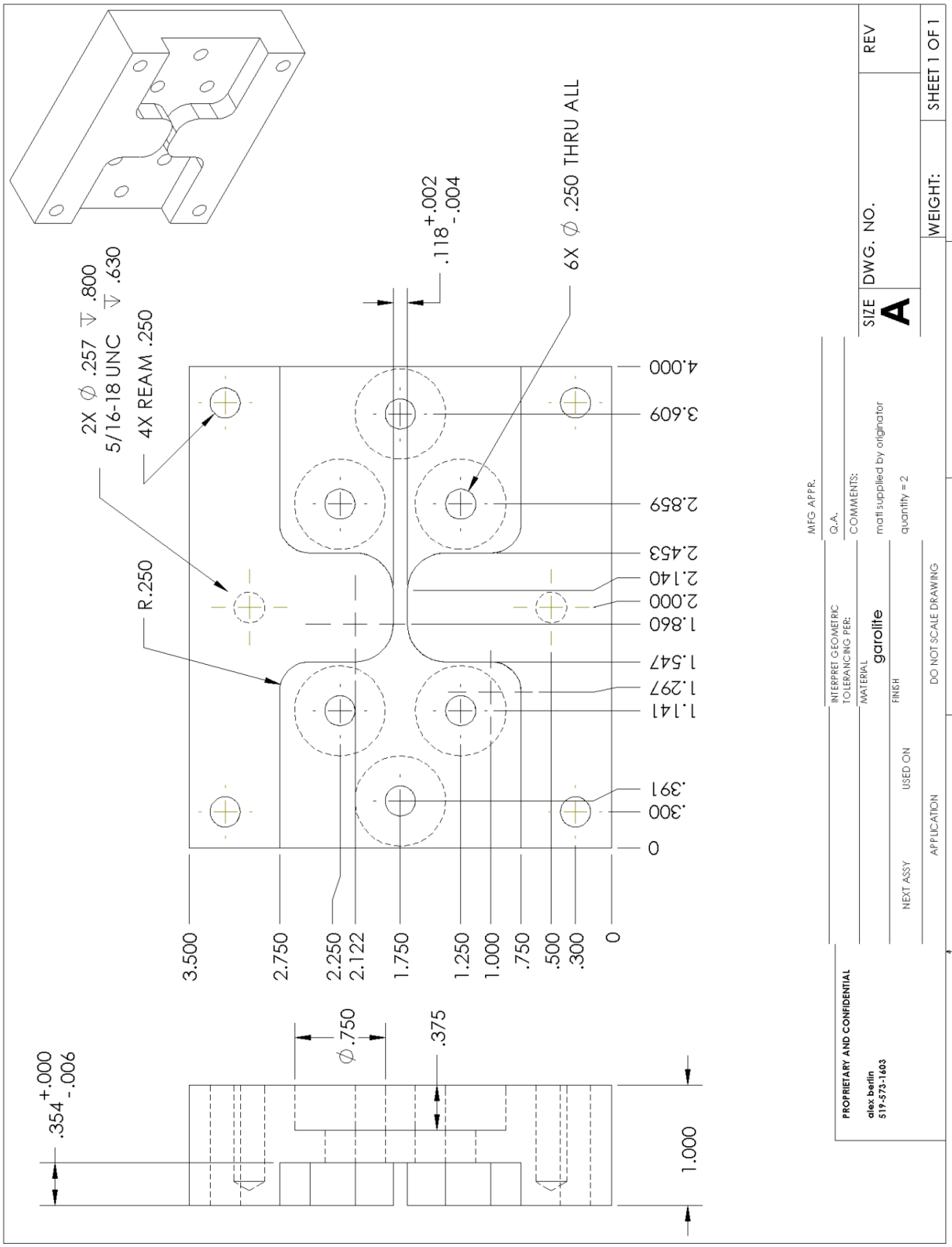
2X ⌀ .257 ▽ .800
5/16-18 UNC ▽ .630
4X REAM .250
R.250
.118 +.002 -.004
6X ⌀ .250 THRU ALL
4.000
3.609
2.859
2.453
2.140
2.000
1.860
1.547
1.297
1.141
.391
.300
0
3.500
2.750
2.250
2.122
1.750
1.250
1.000
.750
.500
.300
0
.354 +.000 -.006
⌀.750
.375
1.000
MFG APPR.
Q.A.
INTERPRET GEOMETRIC TOLERANCING PER:
COMMENTS:
MATERIAL
garolite
matl supplied by originator
FINISH
quantity = 2
NEXT ASSY
USED ON
APPLICATION
DO NOT SCALE DRAWING
PROPRIETARY AND CONFIDENTIAL
alex berlin
519-573-1603
SIZE
A
DWG. NO.
REV
WEIGHT:
SHEET 1 OF 1